

Spectrum of passive scalar carried by particles in isotropic turbulence

Izumi Saito^{*} and Takeshi Watanabe[†]

Department of Engineering, Nagoya Institute of Technology, Nagoya 466-8555, Japan

Toshiyuki Gotoh[‡]

*Department of Engineering, Nagoya Institute of Technology, Nagoya 466-8555, Japan
and Research and Education Center for Natural Sciences, Keio University,
Hiyoshi, Yokohama 223-8521, Japan*



(Received 13 April 2023; accepted 3 April 2024; published 3 May 2024)

We conducted numerical simulations of passive scalar carried by noninertial particles convected by the isotropic turbulence at low to high Reynolds number up to $R_\lambda = 550$ with infinitely large Schmidt numbers. In the numerical method, each particle has a scalar value θ_p that relaxes with a relaxation time τ_θ independent of the turbulence and its evolution is computed along the Lagrangian trajectory, and the scalar is mapped onto the Eulerian grid points. In the limit of large τ_θ , the evolution equation for the mapped field θ converges to that in the Batchelor regime with an infinite Schmidt number. We investigated the two point statistics including the variance spectrum of the field θ and confirmed their consistency with the turbulence theory, such as the Batchelor spectrum, constancy of the transfer flux, and the Yaglom 4/3 law for the third-order structure function by parameter sweep simulations with various values of τ_θ . An explanation of the present numerical method from the view point of the turbulence physics is presented. The visualized scalar field shows features commonly seen in passive scalar turbulence, such as plateaus, fronts, and sheetlike structures.

DOI: [10.1103/PhysRevFluids.9.054601](https://doi.org/10.1103/PhysRevFluids.9.054601)

I. INTRODUCTION

Turbulent transfer of small particles plays important roles in many natural phenomena and engineering applications, such as aerosols, rain drops in clouds, dust particles from volcanic eruptions, and spraying of chemical fertilizer. The spatial distribution of various properties of particles (such as number, mass, and temperature) can be regarded as a continuum of scalar field from macroscopic view point which describes phenomena at scales much larger than the mean distance between particles [1]. This continuum of the scalar shares some characteristics with those of scalar such as temperature, concentration like salinity and chemicals in that both are convected by turbulent flow, but the latter undergoes the molecular diffusion, while the former has almost zero molecular diffusivity. This is because the typical radius of particles above is larger than 1 or sub micron meter for which the estimated diffusivity in terms of the Einstein formula is much smaller than that of gases or temperature [2]. Therefore the continuum of scalar as ensemble of very tiny particles corresponds to the scalar with very high or infinite Schmidt number $Sc = \nu/\kappa \gg 1$.

^{*}izumi@gfd-dennou.org

[†]watanabe@nitech.ac.jp

[‡]gotoh.toshiyuki@nitech.ac.jp

Transport and mixing of passive scalar at high Schmidt number convected by turbulent flow is one of the canonical problems in turbulence research and has long been studied since Batchelor's pioneering work [3]. His theory predicts that when the Reynolds number and Schmidt number are large the variance spectrum which is defined by

$$\langle \theta^2 \rangle = \int_0^\infty E_\theta(k) dk \quad (1)$$

has two power-law scaling ranges as

$$E_\theta(k) = \begin{cases} C_{OC} \bar{\chi} \bar{\epsilon}^{-1/3} k^{-5/3} & \text{for } k_L \ll k \ll k_d, \\ C_B \bar{\chi} (\bar{\epsilon}/\nu)^{-1/2} k^{-1} & \text{for } k_d \ll k \ll k_B, \end{cases} \quad (2)$$

where the angle brackets $\langle \rangle$ denote the ensemble average, C_{OC} and C_B are the Obukhov-Corrsin constant [4,5] and the Batchelor constant, respectively, and $k_L, k_d = (\bar{\epsilon}/\nu^3)^{1/4}$, and $k_B = Sc^{1/2} k_d$ are the inverse of the integral scale, the Kolmogorov and the Batchelor wave numbers, respectively. The $\bar{\epsilon}$ and $\bar{\chi}$ are the means of the kinetic energy dissipation rate and the destruction rate of the scalar variance (hereafter we denote simply scalar dissipation rate), respectively. Many efforts have been made for examining the predictions by experiment [6–8], theory [9–12], and direct numerical simulation (DNS) [13–17]. The Obukhov-Corrsin constant is found to be about 0.6-0.7 at high Reynolds number for $Sc = O(1)$. However, the Batchelor constant is difficult to pin down compared to the Obukhov-Corrsin constant because k_B is proportional to $Sc^{1/2}$ so that very high resolution for the scalar is necessary to find the k^{-1} spectrum regardless of experiment [8] or DNS. DNSs with very large number of grid points up to 8192^3 and $Sc = 512$ have been conducted, and the Batchelor spectrum, recover of isotropy at small scales and saturation of the scaling exponents of the structure functions of the scalar increments are reported [18,19]. $Sc = 512$ is large, but smaller than those of some scalars such as salinity and so on. Since DNS for high Sc is very demanding in the computational resources, alternative methods should be explored.

One important aspect regarding the k^{-1} spectrum (hereafter the Batchelor spectrum) is that when $Sc \gg 1$ the k^{-1} spectrum exists for $k \gg k_d$ irrespective of the Reynolds number. In other words, the scale separation between turbulent velocity and scalar fluctuations is essential and necessary. With this understanding, a hybrid method using the dual grid system was proposed by one of the present authors. In the method, the velocity at low to moderate Reynolds numbers on the coarse grid is computed by the spectral method, and the passive scalar at high Schmidt numbers on the finer grid is computed by the combined compact finite difference method [20]. The k^{-1} spectrum over the finite range of wave number with $C_B \approx 5.7$ was found at $R_\lambda = 42$, $Sc = 1000$ [21], which is consistent with the value obtained by high resolution DNSs. More sophisticated numerical methods on the same line have been developed to compute the passive scalar at high Schmidt numbers using GPUs, and these methods were found to be very efficient for the present purpose [22,23]. Lagaert *et al.* (2014) [24] proposed the hybrid spectral-particle method which uses the spectral method for velocity fields and the semi-Lagrangian particle method for scalar fields followed by re-meshing and molecular diffusion, allowing the computation of the high but finite Schmidt number scalar turbulence. Götzfried *et al.* [25] studied the mixing of passive scalar in both the Lagrangian and Eulerian frames for $Sc = 1-64$. In the Lagrangian frame, the inertia-less particles subjected to the Wiener process and their trajectory are tracked to compute the concentration. At early times, the scalar variances by the both methods agree to each other, but at latter times the filaments or sheets structure of the concentration in the Lagrangian frame are found to be noisy reflecting the discreteness of the particles. However, even with these methods, it is still difficult to compute the two spectral ranges with finite width at high Schmidt and high Reynolds numbers [17]. More efficient and effective computational method is necessary to explore various statistical properties of the scalar fluctuations in this range.

Difficulty in the Eulerian computation lies in the resolution criterion $k_{\max} > k_B = Sc^{1/2} k_d \gg k_d$ and the associated condition for the time step width which are very stringent. A hint to overcome the

barrier is to use a fully Lagrangian description of scalar carried by particle, and to map those scalar onto the Eulerian grids. Unlike the semi-Lagrangian particle method by Ref. [24], in which the fluid particle is tracked over short time step and the scalar on the particle is mapped onto the grids, in the present method, the particle position and the evolution of the scalar on the particle are tracked all the way along the particle trajectory, and the scalar amplitudes are mapped onto the surrounding grid points, giving the Eulerian distribution. This resembles the measurement of the spectrum of the liquid water content (LWC) in cloud. Cloud droplets which are convected by turbulent flow with almost zero molecular diffusion carry the water mass (Lagrangian picture), however, the measurement of the power spectrum is made by the detector mounted on the measurement tower (Eulerian picture) with finite resolution in space and time, which corresponds to a mapping of the scalar (water mass) onto the grid (detector) in time.

Motivated by this analogy, in the recent study, hereafter referred to as GSW21 [26], we developed a new numerical simulation method of point particles with thermal inertia that are passively advected by turbulence, and investigated the variance spectrum of the particle thermal energy in the wave-number space. The spectrum showed $k^{-5/3}$ and k^{-1} at lower and higher wave numbers, respectively, which is consistent with the turbulence theory. However, the spectrum suffered from significant noise at larger wave numbers due to a lack of statistical convergence (see Fig. 2 in GSW21), which made the reliability of the result unclear, and the examination of the properties of the method in both physical and numerical view points was not sufficient.

In the present study, we extend the GSW21 study to conduct a more careful and comprehensive investigation of the new method with special emphasis on the relation between the numerical method and the physics of turbulence, namely about the transfer flux of the scalar variance through the spectral space and the scalar dissipation, removal of the shot noise, and coarse graining of the Lagrangian information by the mapping onto the Eulerian grids. To make the points clearer, we consider a simple idealized model, a passive scalar θ_p carried by the noninertial particles in isotropic turbulence at high Reynolds and Schmidt numbers. We examine the statistical properties of the scalar field θ as the mapped field of θ_p for which we refer it as the ‘‘particle field’’ [27]. We perform parameter sweep simulations with a relatively moderate number of particles and grid points, and investigate various turbulence statistics such as the variance spectrum, transfer flux, and structure function. And we also conduct large-scale simulations with grid points up to 2048^3 and Reynolds number $R_\lambda = 550$ for comparison with the Batchelor theory. The transfer flux in the wave-number space and the dissipation are theoretically examined in both the Eulerian and Lagrangian view points.

The remainder of this paper is organized as follows. Section II presents the governing equations. Section III reviews the theory by GSW21. Sections IV and V provide the simulation setup and results, respectively, for moderate-scale simulations. Section VI provides the results for large-scale simulations. Section VII discusses the transfer flux and the scalar dissipation. Finally, Sec. VIII gives a summary and discussion.

II. GOVERNING EQUATIONS

The velocity field for a fluid is governed by the incompressible Navier-Stokes equations:

$$\frac{\partial \mathbf{u}}{\partial t} + \mathbf{u} \cdot \nabla \mathbf{u} = -\frac{\nabla p}{\rho_0} + \nu \nabla^2 \mathbf{u} + \mathbf{f}, \quad (3)$$

$$\nabla \cdot \mathbf{u} = 0, \quad (4)$$

where p is the pressure; ρ_0 is the constant mass density of the fluid; and \mathbf{f} represents the external force, which is solenoidal ($\nabla \cdot \mathbf{f} = 0$). We consider N_p point particles that move in the same way as fluid particles. The evolution equation for the j th particle position, \mathbf{x}_{pj} , is given by

$$\frac{d\mathbf{x}_{pj}}{dt} = \mathbf{u}(\mathbf{x}_{pj}, t), \quad (5)$$

where $\mathbf{u}(\mathbf{x}_{pj}, t)$ is the fluid velocity at \mathbf{x}_{pj} at time t . We consider that each particle has a passive scalar $\theta_{pj}(t)$, the evolution equation of which is given by

$$\frac{d\theta_{pj}}{dt} = -\frac{\theta_{pj}}{\tau_\theta} + f_\theta(\mathbf{x}_{pj}, t), \quad (6)$$

where τ_θ is a constant parameter representing the relaxation time for θ_{pj} and $f_\theta(\mathbf{x}_{pj}, t)$ is the value of a certain fluid field f_θ at \mathbf{x}_{pj} at time t . Originally, Eq. (6) comes from the evolution equation for the temperature of a particle with thermal inertia, and τ_θ corresponds to the thermal relaxation time [28,29]. However, we do not consider such a specific physical correspondence in this study. We regard the present system as an idealized system for the study of spectrum of the particle field in turbulence.

III. THEORY

It is important for the latter arguments to examine the physical properties of Eq. (6) in the Eulerian framework, although its actual computation is made in the Lagrangian frame. We consider the particle field $\theta(\mathbf{x}, t)$, which is defined as the spatial distribution of the scalar $\theta_{pj}(t)$ as follows [30–32]:

$$\theta(\mathbf{x}, t) = \frac{1}{n_0} \sum_{j=1}^{N_p} \theta_{pj}(t) \delta(\mathbf{x} - \mathbf{x}_{pj}), \quad (7)$$

where $\delta()$ is the Dirac δ function, n_0 is the mean number density of particles in the domain,

$$n_0 = \frac{N_p}{V}, \quad (8)$$

and V is the domain volume. Because particles are advected by a fluid in the same way as fluid particles, and the scalar θ_{pj} is relaxed with a time constant τ_θ and is affected by f_θ as in Eq. (6), the evolution equation for $\theta(\mathbf{x}, t)$ as a scalar continuum is given by

$$\frac{\partial \theta}{\partial t} + \mathbf{u} \cdot \nabla \theta = -\frac{\theta}{\tau_\theta} + f_\theta, \quad (9)$$

in the limit of $n_0 \rightarrow \infty$. Note that this equation does not have the molecular diffusion term ($\kappa \nabla^2 \theta$) in this case. When the coarse graining over some spatial domain is made, a diffusive type term emerges as the reflection of the coarse graining [2], but for the moment we proceed as the zero diffusivity. Effects of the finiteness of the number density will be discussed in the latter section. Thus, if we assume f_θ as the external scalar source, Eq. (9) is the equation for a passive scalar field at $Sc = \infty$, which is modified by the relaxation term with τ_θ .

It was shown in GSW21 that the Batchelor spectrum in the viscous-convective range is modified by the relaxation term as

$$E_\theta(k) = C_B \bar{\chi}_{\text{in}} (\bar{\epsilon}/\nu)^{-1/2} k^{-1} (k\eta)^{-\alpha}, \quad (10)$$

$$\alpha = (2C_B) D_K, \quad (11)$$

where $\eta = k_d^{-1}$ is the Kolmogorov scale,

$$D_K = \tau_K / \tau_\theta, \quad (12)$$

and $\tau_K = (\bar{\epsilon}/\nu)^{-1/2}$ is the Kolmogorov time. In addition, when the Reynolds number is large and the parameter D_L defined by

$$D_L = T / \tau_\theta \quad (13)$$

is much smaller than unity, the two power-law ranges exist as

$$E_\theta(k) = \begin{cases} C_{OC} \bar{\chi}_{in} \bar{\epsilon}^{-1/3} k^{-5/3} & \text{for } k \ll k_d, \\ C_B \bar{\chi}_{in} (\bar{\epsilon}/\nu)^{-1/2} k^{-1} (k\eta)^{-\alpha} & \text{for } k \gg k_d, \end{cases} \quad (14)$$

where T is the large-eddy turnover time of turbulence, C_{OC} and C_B are the Obukhov-Corrsin constant and the Batchelor constant, respectively, and $\bar{\chi}_{in}$ is the mean scalar fluctuation injection rate. The two ranges cross over at the wave number k_d . The $k^{-1-\alpha}$ is the modified Batchelor spectrum and its derivation is explained in GSW21. The essence of the derivation is the fact that the velocity field convecting the scalar in this range is approximated by the linear function of the coordinates with the uniform velocity gradient in the Eulerian representation, i.e., $\mathbf{u} \rightarrow \mathbf{A} \cdot \mathbf{x}$ where $\mathbf{A} = \nabla \mathbf{u}$. Equation (10) shows that the relaxation term modifies the Batchelor spectrum and changes its slope from -1 to $-1 - \alpha$, where $\alpha = (2C_B)D_K$. For $\tau_\theta \rightarrow \infty$, $D_K \rightarrow 0$ and $\alpha \rightarrow 0$, hence the convergence to the Batchelor spectrum.

IV. SIMULATION SETUP

We conduct numerical simulations of particles in turbulence using a DNS model developed for the large-scale computation of particle-laden turbulent flow [33,34]. The numerical domain is a periodic cubic box with a length L_{box} per side (i.e., $V = L_{\text{box}}^3$). Particles are regarded as point particles. The fluid velocity and the external source f_θ at the particle position, $\mathbf{u}(\mathbf{x}_{pj})$ and $f_\theta(\mathbf{x}_{pj})$, are calculated from \mathbf{u} and f_θ fields at the surrounding eight grid points by linear interpolation, respectively. We numerically integrate the evolution equations (3)–(6) using the pseudospectral method for spatial discretization and the second-order Runge-Kutta scheme for temporal discretization with time increment $\Delta t = 1.0 \times 10^{-3}$.

Because the domain length in the present simulation is L_{box} , each component of the wave-number vector $\mathbf{k} = (k_1, k_2, k_3)$ ($k = |\mathbf{k}|$) is defined as $k_i = (2\pi/L_{\text{box}}) \times (\text{integer})$ ($i = 1, 2, 3$), which is not an integer in general. In the following simulation and data analysis, we also use the integer wave number defined by

$$k'_i = k_i L_{\text{box}} / (2\pi), \quad (15)$$

where $\mathbf{k}' = (k'_1, k'_2, k'_3)$ and $k' = |\mathbf{k}'|$.

The velocity forcing \mathbf{f} satisfies

$$\langle \mathbf{f}(\mathbf{k}', t) \mathbf{f}(-\mathbf{k}', s) \rangle = \mathbf{P}(\mathbf{k}') \frac{F(k')}{4\pi(k')^2} \delta(t - s), \quad (16)$$

where \mathbf{P} is the projection operator [$P_{ij} = \delta_{ij} - k'_i k'_j / (k')^2$], and the spectrum of the force $F(k')$ is constant ($= c_f$) for $1 \leq k' \leq 2$ and zero otherwise [35]. Similarly, the scalar forcing f_θ satisfies

$$\langle f_\theta(\mathbf{k}', t) f_\theta(-\mathbf{k}', s) \rangle = \frac{F_\theta(k')}{4\pi(k')^2} \delta(t - s), \quad (17)$$

where $F_\theta(k')$ is constant ($= c_\theta$) for $1 \leq k' \leq 2$ and zero otherwise. We tune the parameters c_f and c_θ so that the mean dissipation rates for the kinetic energy ($\bar{\epsilon}$) and scalar variance ($\bar{\chi}$) are as given in Tables II and III, respectively.

Table I summarizes various parameters used in the present simulation. Tables II and III summarize the turbulence parameters for the fluid velocity field and the particle field, respectively (see Appendix A for definitions of turbulence parameters). We first conduct four kinds of simulations: Runs A–D (see Table I). Runs A and B use the same number of grids cells $N_{\text{grid}} = 128^3$, but Run B has higher resolution with the kinematic viscosity ν being twice that for Run A. Run C uses $N_{\text{grid}} = 256^3$ and has a higher Reynolds number R_λ . For Runs A–C, we conduct simulations with six values of τ_θ (from $\tau_\theta = 200$ to 11.1, referred to as A1–A6, B1–B6, and C1–C6) to examine the dependence on the parameter D_K . Run D is for visualization. We also conduct large-scale

TABLE I. Parameters used in the simulations. From left to right, N_{grid} is the total number of grid cells for the fluid velocity field \mathbf{u} and the particle field $\tilde{\theta}$, N_p is the total number of particles, N_p/N_{grid} is the number of particles per grid cell, ν is the kinematic viscosity, L_{box} is the box length, Δx is the grid cell length, τ_θ is the relaxation time, n_0 is the mean particle number density, and $\Delta x_p = n_0^{-1/3}$ is the average distance of particles.

Run	N_{grid}	N_p	N_p/N_{grid}	ν	L_{box}	Δx	τ_θ	n_0	Δx_p
A1–A6	128^3	2^{27}	64	0.15	25.6	0.2	200 (A1), 100 (A2) 33.3 (A3), 20.0 (A4) 14.3 (A5), 11.1 (A6)	8000	0.050
B1–B6	128^3	2^{29}	256	0.30	25.6	0.2	200 (B1), 100 (B2) 50.0 (B3), 33.3 (B4) 25.0 (B5), 20.0 (B6)	32000	0.031
C1–C6	256^3	2^{29}	32	0.15	51.2	0.2	200 (C1), 100 (C2) 33.3 (C3), 20.0 (C4) 14.3 (C5), 11.1 (C6)	4000	0.063
D1	128^3	2^{30}	512	0.15	25.6	0.2	100	64000	0.025
D2	128^3	2^{26}	32	0.15	25.6	0.2	100	4000	0.063
D3	128^3	2^{22}	2	0.15	25.6	0.2	100	250	0.16
E	1024^3	2^{34}	16	0.15	204.8	0.2	200	2000	0.079
F	2048^3	2^{36}	8	0.15	409.6	0.2	200	1000	0.10

simulations with $N_{\text{grid}} = 1024^3$ and 2048^3 (Runs E and F), the results of which are described later in Sec. VI.

The root-mean-square (rms) value of the particle field, θ_{rms} , is calculated by

$$\theta_{\text{rms}} = \sqrt{\langle \theta_p^2 \rangle_p}, \quad (18)$$

where $\langle \rangle_p$ indicates the average over particles and time ($\langle \theta_p^2 \rangle_p$ is calculated by the time average of $\sum_{j=1}^{N_p} \theta_{pj}^2 / N_p$). The dissipation rate for the particle field, χ , is calculated by

$$\chi = \frac{2}{\tau_\theta} \theta_{\text{rms}}^2 = \frac{2}{\tau_\theta} \langle \theta_p^2 \rangle_p, \quad (19)$$

which is obtained from Eqs. (6), (7), and (9) [see Appendix B for the derivation of Eq. (19)]. As we will argue later in detail in Sec. VII, the scalar fluctuation injection χ_{in} balances the dissipation

TABLE II. Turbulence parameters for statistically steady states. Values are mean \pm standard deviation. Here, R_λ is the Taylor microscale Reynolds number, u_{rms} is the root-mean-square (rms) velocity, $\bar{\epsilon}$ is the mean energy dissipation rate per unit mass, \mathcal{L} is the integral scale, λ is the Taylor microscale, $\bar{\eta}$ is the mean Kolmogorov length, $k_{\text{max}} \bar{\eta}$ is the cutoff wave number normalized by the mean Kolmogorov length, T is the large-eddy turnover time, and τ_K is the Kolmogorov time.

Run	R_λ	u_{rms}	$\bar{\epsilon}$	\mathcal{L}	λ	$\bar{\eta}$	$k_{\text{max}} \bar{\eta}$	T	τ_K
A, D	83 ± 11	5.9 ± 0.5	18 ± 4	5.8 ± 0.4	2.1 ± 0.2	0.12 ± 0.01	1.7 ± 0.1	1.0 ± 0.1	0.093 ± 0.010
B	58 ± 7	5.9 ± 0.5	19 ± 3	6.3 ± 0.4	2.9 ± 0.2	0.20 ± 0.01	2.8 ± 0.1	1.1 ± 0.1	0.13 ± 0.01
C	136 ± 19	7.7 ± 0.6	20 ± 4	11 ± 1	2.6 ± 0.2	0.12 ± 0.01	1.6 ± 0.1	1.5 ± 0.1	0.089 ± 0.009
E	330 ± 60	12 ± 1	17 ± 4	43 ± 4	4.3 ± 0.5	0.12 ± 0.01	1.7 ± 0.1	3.7 ± 0.4	0.097 ± 0.011
F	550 ± 50	15 ± 1	16 ± 1	85 ± 5	5.5 ± 0.3	0.12 ± 0.01	1.7 ± 0.1	5.7 ± 0.2	0.096 ± 0.005

TABLE III. Scalar parameters for statistically steady states. θ_{rms} is the rms value of θ , $\bar{\chi}$ is the mean dissipation rate for the θ variance, D_K is a parameter defined by Eq. (12), and $\delta\alpha$ is the slope deviation described in Fig. 4 (see the text for details). Values are mean \pm standard deviation for θ_{rms} , $\bar{\chi}$, and D_K . Errors in $\delta\alpha$ are estimated by the difference in the maximum and minimum values of $\delta\alpha$ for $5 \leq k'_{\text{ref}} \leq 15$ (see the text for the details of k'_{ref}).

Run	θ_{rms}	$\bar{\chi}$	D_K	$\delta\alpha$
A1	$(1.99 \pm 0.01) \times 10^{-3}$	$(3.97 \pm 0.02) \times 10^{-8}$	$(4.7 \pm 0.5) \times 10^{-4}$	0
A2	$(2.00 \pm 0.01) \times 10^{-3}$	$(8.04 \pm 0.09) \times 10^{-8}$	$(9.3 \pm 1.0) \times 10^{-4}$	$(5.9 \pm 1.7) \times 10^{-3}$
A3	$(2.01 \pm 0.03) \times 10^{-3}$	$(2.43 \pm 0.07) \times 10^{-7}$	$(2.8 \pm 0.3) \times 10^{-3}$	$(2.7 \pm 0.4) \times 10^{-2}$
A4	$(2.01 \pm 0.04) \times 10^{-3}$	$(4.04 \pm 0.02) \times 10^{-7}$	$(4.7 \pm 0.5) \times 10^{-3}$	$(4.8 \pm 0.4) \times 10^{-2}$
A5	$(2.01 \pm 0.05) \times 10^{-3}$	$(5.64 \pm 0.03) \times 10^{-7}$	$(6.5 \pm 0.7) \times 10^{-3}$	$(6.9 \pm 0.5) \times 10^{-2}$
A6	$(2.01 \pm 0.05) \times 10^{-3}$	$(7.27 \pm 0.04) \times 10^{-7}$	$(8.4 \pm 0.9) \times 10^{-3}$	$(8.9 \pm 0.6) \times 10^{-2}$
B1	$(2.01 \pm 0.01) \times 10^{-3}$	$(4.03 \pm 0.05) \times 10^{-8}$	$(6.5 \pm 0.5) \times 10^{-4}$	0
B2	$(2.02 \pm 0.02) \times 10^{-3}$	$(8.14 \pm 0.15) \times 10^{-8}$	$(1.3 \pm 0.1) \times 10^{-3}$	$(7.6 \pm 0.1) \times 10^{-3}$
B3	$(2.02 \pm 0.03) \times 10^{-3}$	$(1.64 \pm 0.05) \times 10^{-7}$	$(2.6 \pm 0.2) \times 10^{-3}$	$(2.3 \pm 0.2) \times 10^{-2}$
B4	$(2.02 \pm 0.04) \times 10^{-3}$	$(2.46 \pm 0.11) \times 10^{-7}$	$(3.9 \pm 0.3) \times 10^{-3}$	$(3.8 \pm 0.2) \times 10^{-2}$
B5	$(2.02 \pm 0.05) \times 10^{-3}$	$(3.27 \pm 0.17) \times 10^{-7}$	$(5.2 \pm 0.4) \times 10^{-3}$	$(5.2 \pm 0.2) \times 10^{-2}$
B6	$(2.01 \pm 0.04) \times 10^{-3}$	$(4.06 \pm 0.16) \times 10^{-7}$	$(6.5 \pm 0.5) \times 10^{-3}$	$(6.7 \pm 0.3) \times 10^{-2}$
C1	$(1.99 \pm 0.01) \times 10^{-3}$	$(3.94 \pm 0.02) \times 10^{-8}$	$(4.4 \pm 0.4) \times 10^{-4}$	0
C2	$(2.00 \pm 0.01) \times 10^{-3}$	$(8.01 \pm 0.07) \times 10^{-8}$	$(8.9 \pm 0.9) \times 10^{-4}$	$(5.3 \pm 0.6) \times 10^{-3}$
C3	$(2.00 \pm 0.02) \times 10^{-3}$	$(2.40 \pm 0.06) \times 10^{-7}$	$(2.7 \pm 0.3) \times 10^{-3}$	$(2.6 \pm 0.2) \times 10^{-2}$
C4	$(2.00 \pm 0.04) \times 10^{-3}$	$(4.00 \pm 0.15) \times 10^{-7}$	$(4.4 \pm 0.4) \times 10^{-3}$	$(4.7 \pm 0.3) \times 10^{-2}$
C5	$(2.00 \pm 0.05) \times 10^{-3}$	$(5.60 \pm 0.27) \times 10^{-7}$	$(6.2 \pm 0.6) \times 10^{-3}$	$(6.6 \pm 0.3) \times 10^{-2}$
C6	$(2.00 \pm 0.06) \times 10^{-3}$	$(7.23 \pm 0.42) \times 10^{-7}$	$(8.0 \pm 0.8) \times 10^{-3}$	$(8.5 \pm 0.5) \times 10^{-2}$
E	$(1.94 \pm 0.02) \times 10^{-3}$	$(3.76 \pm 0.09) \times 10^{-8}$	$(4.9 \pm 0.6) \times 10^{-4}$	
F	$(1.93 \pm 0.01) \times 10^{-3}$	$(3.71 \pm 0.03) \times 10^{-8}$	$(4.8 \pm 0.3) \times 10^{-4}$	

rate χ in steady state. The balance between χ_{in} and χ is also confirmed in the present simulation as described in Fig. 17.

All results presented in the following section are obtained after each simulation achieves a statistically steady state. This requires a long integration time, especially for simulations with large τ_θ . For simulations with $\tau_\theta = 200$ (Runs A1, B1, and C1), we integrated over 400 nondimensional time units, corresponding to 40 million time steps with $\Delta t = 10^{-3}$ and to 250 large-eddy turnover time for Run C1. After a statistically steady state is achieved for each simulation, we further conduct time integration for 50 nondimensional time units and calculate the time average of various statistics, such as the variance spectrum.

Runs A1–A6 use the same initial conditions for the fluid velocity field and particles, and also use the same series of random numbers for the external forces. The only difference among Runs A1–A6 is the relaxation time τ_θ . Runs B1–B6 and Runs C1–C6 are conducted in the same way. This is important for an accurate estimation of $\delta\alpha$ from the variance spectrum, as later shown in Fig. 3.

V. SIMULATION RESULTS

A. Defiltering and removal of shot noise

To calculate various turbulence statistics for the particle field, we first need to obtain the field $\theta(\mathbf{x}, t)$ in Eq. (7) from particle data. This is not straightforward because Eq. (7) includes the Dirac δ function. In the present study, we follow the method reported by Ref. [34] and simply project the particle information onto the surrounding eight grid points of the fluid field using the linear weight

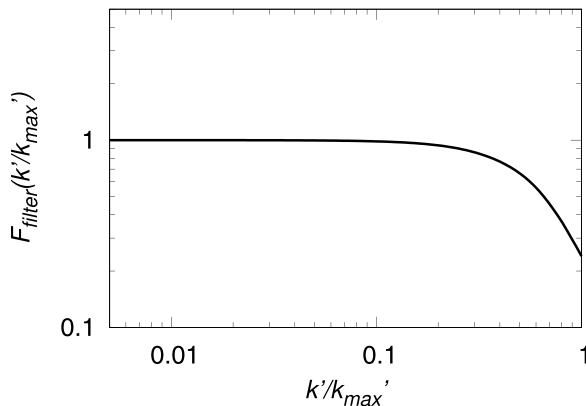


FIG. 1. The filtering effect F_{filter} [defined in Eq. (C1)] is a function of k'/k'_{max} , where k'_{max} is the cutoff wave number ($k'_{\text{max}} = 128$ for $N_{\text{grid}} = 256^3$).

as follows:

$$\tilde{\theta}(\mathbf{x}, t) = \frac{1}{n_0} \sum_{j=1}^{N_p} \theta_{pj} S(\mathbf{x}, \mathbf{x}_{pj}), \quad (20)$$

where the tilde indicates that $\tilde{\theta}(\mathbf{x}, t)$ is an approximation for $\theta(\mathbf{x}, t)$, and the operator $S(\mathbf{x}, \mathbf{x}_{pj})$ projects the particle information at \mathbf{x}_{pj} onto \mathbf{x} based on the linear weight [36].

The variance spectrum for $\tilde{\theta}$ is defined by

$$\langle \tilde{\theta}^2 \rangle = \int_0^\infty E_{\tilde{\theta}}(k) dk. \quad (21)$$

The spectrum $E_{\tilde{\theta}}(k)$ can be decomposed into three parts as follows [30,34,37,38]:

$$E_{\tilde{\theta}}(k) = F_{\text{filter}}(k) [E_{\theta}(k) + E_{\theta}^{\text{shot}}(k)]. \quad (22)$$

First, $F_{\text{filter}}(k)$ is a function for the filtering effect of the projection. The projection of the particle information onto surrounding grid points has a low-pass filtering effect because the particle position spatial accuracy is lost for scales smaller than the grid cell length Δx . Figure 1 shows $F_{\text{filter}}(k)$, where its form was estimated by the method previously reported [34]. The fitting function for $F_{\text{filter}}(k)$ is provided in Appendix C. Next, $E_{\theta}^{\text{shot}}(k)$ arises from the discreteness of particles in the θ field and corresponds to a spatially uncorrelated distribution. The derivation of this uncorrelated part is as previously described [34]. $E_{\theta}^{\text{shot}}(k)$ is given by

$$E_{\theta}^{\text{shot}}(k) = n_0^{-1} \langle \theta_p^2 \rangle_p \frac{(4\pi k^2)}{V}, \quad (23)$$

where the proportionality to k^2 originates from the Fourier transform of the Dirac δ function. Physically, this part corresponds to shot noise in electronics, which originates from the discrete nature of electric charge. Based on this similarity, we refer to $E_{\theta}^{\text{shot}}(k)$ as shot noise spectrum. Finally, $E_{\theta}(k)$ describes the spatial coherency of the θ field. The spatial structure of the θ field as a continuum scalar field is reflected in this part. From (22), we calculate $E_{\theta}(k)$ by

$$E_{\theta}(k) = F_{\text{filter}}(k)^{-1} E_{\tilde{\theta}}(k) - E_{\theta}^{\text{shot}}(k). \quad (24)$$

Figure 2 shows the various spectra described above for Run C1.

To calculate other turbulence statistics, such as the transfer flux and structure function, we simply extend the above procedure to remove the filtering effect from the field $\tilde{\theta}(\mathbf{k}, t)$, where $\tilde{\theta}(\mathbf{k}, t) =$

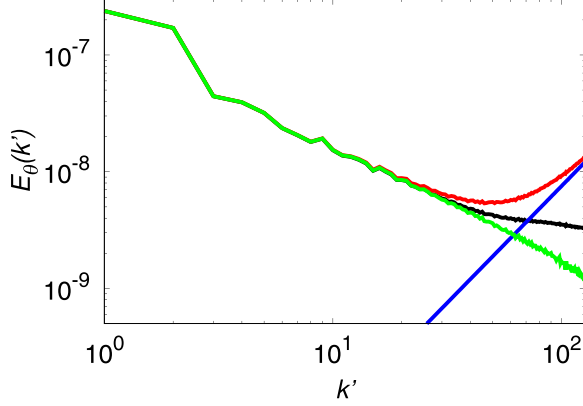


FIG. 2. Variance spectrum of particle field for Run C1 in statistically steady state. Black curve: variance spectrum calculated from raw data $[E_{\tilde{\theta}}(k)]$. Red curve: spectrum without filtering effect $[F_{\text{filter}}(k)^{-1}E_{\tilde{\theta}}(k)]$. Green curve: spectrum without effects of filtering and shot noise spectrum $[E_{\theta}(k)]$. Blue curve: shot noise $[E_{\theta}^{\text{shot}}(k)]$.

$\mathcal{F}[\tilde{\theta}(\mathbf{x}, t)]$ and $\mathcal{F}^{-1}[\]$ indicate the Fourier transform and its inverse, respectively. Instead of using $\tilde{\theta}(\mathbf{x}, t)$, we use

$$\mathcal{F}^{-1}[F_{\text{filter}}(k)^{-1/2} \tilde{\theta}(\mathbf{k}, t)] \quad (25)$$

to calculate the transfer flux and structure function.

B. Convergence to Batchelor spectrum

Figure 3(a) shows the variance spectra $E_{\theta}(k)$ for Runs C1, C2, C4, and C6. Here, each spectrum is normalized using Kolmogorov-Obkhov-Corrsin (KOC) theory as

$$E_{\theta}(k) = \bar{\chi} (\bar{\epsilon})^{-3/4} \nu^{5/4} \hat{E}_{\theta}(k\bar{\eta}), \quad (26)$$

where \hat{E}_{θ} indicates the normalized spectrum. The slopes of the spectra are close to -1 and shallower for runs with smaller D_K (from bottom to top in the panel). The results for Runs C2 (blue) and C1 (green) are almost indistinguishable, indicating convergence. Figure 3(b) is the same as Fig. 3(a), but each spectrum is compensated by $(k\bar{\eta})^{-1}$. The results for Runs C1 and C2 are almost horizontal and agree well with the dashed horizontal line, which is the Batchelor constant $C_B = 5.9$ estimated from Fig. 6 as described later.

We note two points here. First, turbulence theory predicts that the Batchelor spectrum with a slope of -1 will appear for $k\bar{\eta} \gg 1$. However, Fig. 3 shows that the slope is already close to -1 at least from $k\bar{\eta} > 0.04$. Although this seems to be a contradiction, previous studies have also shown that the -1 slope actually appears from $k\bar{\eta} < 1$. GSW21 obtained results similar to those in Fig. 3. They argued that the transition wave number k_* between the Obukhov-Corrsin spectrum and the Batchelor spectrum can be uniquely determined as $k_*\bar{\eta} \sim (C_{OC}/C_B)^{3/2}$, where C_{OC} is the Obukhov-Corrsin constant, and estimated that $k_*\bar{\eta} = 0.038$, which is much smaller than unity. A recent laboratory experiment also reported that a slope of -1 appears for $k\bar{\eta} > 0.03$ [8]. Therefore, we conclude that the result in Fig. 3 shows the Batchelor spectrum and its modification by the relaxation term. Second, it is expected from the theory (10) that the spectrum has a constant slope and becomes shallower as it approaches k^{-1} for smaller D_K . However, the simulation results show that the slope is actually not constant. The spectrum is shallower for smaller D_K , but finally becomes even shallower than k^{-1} for smallest D_K runs (Runs C1 and C2, especially for $0.05 < k\bar{\eta} < 0.2$). This suggests the possibility that the scalar variance spectrum at the limit $D_K = 0$ takes the form $E_{\theta}(k) \propto k^{-1+\delta(k)}$, where $\delta(k)$ is a function indicating the deviation of the slope from -1 . Figure 3(b)

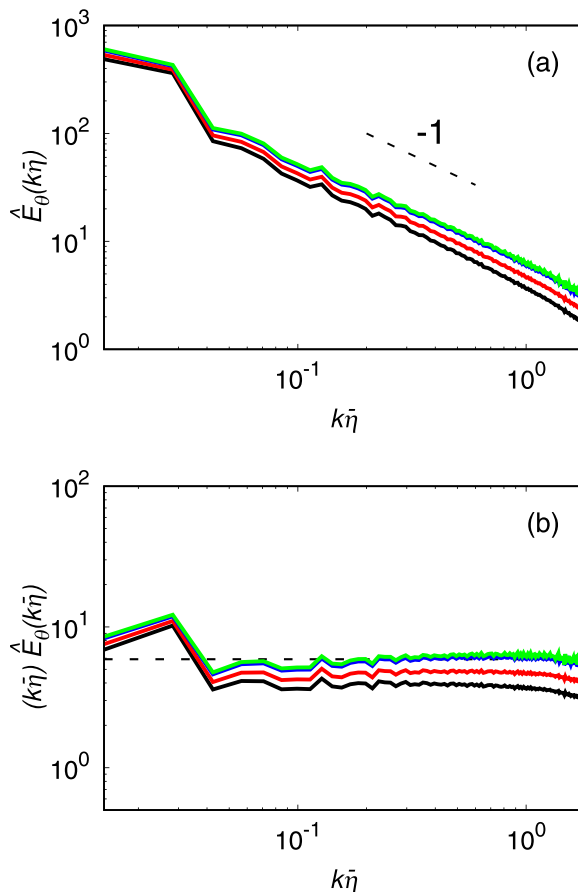


FIG. 3. (a) Normalized variance spectrum of particle field for Runs C1 (green), C2 (blue), C4 (red), and C6 (black) in statistically steady state. Dashed line indicates k^{-1} . (b) Same as (a) but each spectrum is compensated by $(k\bar{\eta})^{-1}$. The dashed horizontal line indicates the Batchelor constant $C_B = 5.9$ estimated from Fig. 6(b).

suggests that $\delta(k)$ is positive and decreasing function of $k\bar{\eta}$, and likely to tend to zero for even greater $k\bar{\eta}$. We are not sure whether $\delta(k)$ is universal, and whether it depends on other parameters such as Reynolds number. Clarifying these characteristics is an important task, but is beyond the scope of this work.

We next investigate the slope of the compensated spectrum, α . The simplest way is to directly estimate α from each spectrum in Fig. 3(b). However, this causes ambiguity in the estimation of α since the spectrum slope is not constant. To avoid this ambiguity, we use the concept of the slope deviation $\Delta\alpha$ as described below. Here, we assume that the deviation $\delta(k)$ does not depend on D_K and that the scalar variance spectrum is modified by the relaxation term in a similar manner as in Eq. (10), namely,

$$\frac{E_\theta(k)|_{D_K>0}}{E_\theta(k)|_{D_K=0}} \propto \frac{k^{-1+\delta(k)-\alpha}}{k^{-1+\delta(k)}} = k^{-\alpha}, \quad (27)$$

when the other parameters such as Reynolds number are unchanged. The following explanation is for Run C, but the procedure is similar for Runs A and B.

Figure 4 shows a schematic of the procedure. First, we use the spectrum with the smallest D_K (for Run C1) as a reference spectrum. Figure 4(a) compares the compensated spectra, $kE_\theta(k)$, for

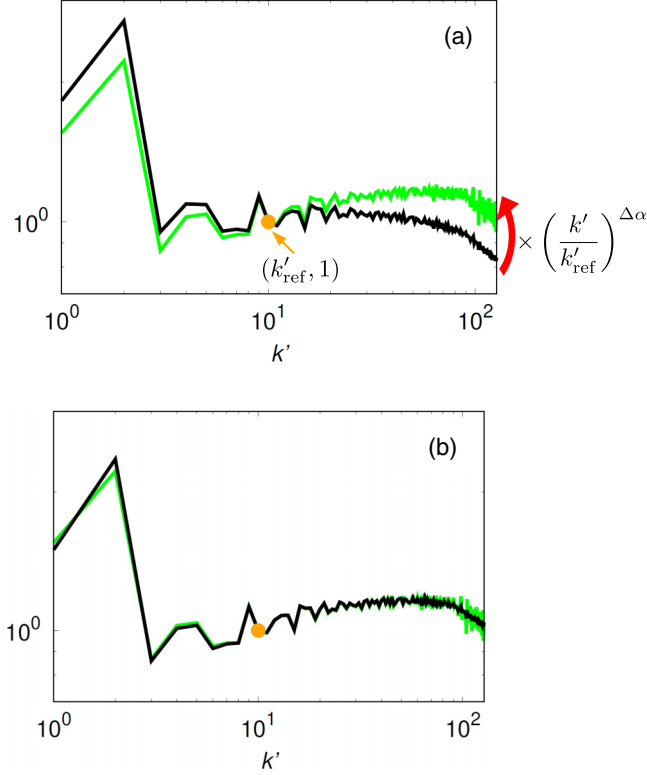


FIG. 4. Schematic of procedure to estimate slope deviation $\Delta\alpha$ of scalar variance spectrum for Run C6 (black) as compared to that for Run C1 (green, reference spectrum). (a) Each spectrum is multiplied by a constant so that its value at the reference wave number $k'_{\text{ref}} = 10$ is unity (orange dot). Then, the spectrum for Run C6 (black) is multiplied by $(k'/k'_{\text{ref}})^{\Delta\alpha}$ (red arrow) so that the result agrees with the reference spectrum. (b) As a result, the two spectra agree.

Runs C1 and C6, where each spectrum is multiplied by a constant so that its value at the reference wave number $k' = k'_{\text{ref}}$ is unity (orange dot in the panel). Here, we use $k'_{\text{ref}} = 10$ (see Appendix D for an explanation of this choice). Next, we multiply the spectrum for Run C6 by $(k'/k'_{\text{ref}})^{\Delta\alpha}$, and determine $\Delta\alpha$ so that the result agrees with the reference spectrum. Here, we use the following estimator to evaluate the degree of disagreement between two spectra $E_1(k')$ and $E_2(k')$:

$$J = \sum_{k'=k'_{\text{ref}}+1}^{k'_{\text{max}}} \frac{\max[E_1(k'), E_2(k')]}{\min[E_1(k'), E_2(k')]} \quad (28)$$

where k'_{max} is the cutoff wave number ($k'_{\text{max}} = 128$ for $N_{\text{grid}} = 256^3$). We use an iteration method (bisection method) to determine $\Delta\alpha$, which minimizes J . For Run C6, $\Delta\alpha$ is determined as $\Delta\alpha = 8.5 \times 10^{-2}$. Figure 4(b) shows that, after multiplication by $(k'/k'_{\text{ref}})^{\Delta\alpha}$, the spectrum for Run C6 agrees with the reference spectrum. Applying the same procedure, we obtain $\Delta\alpha$ for Runs C2–C5 as well. We set $\Delta\alpha = 0$ for Run C1.

Table III (5th column) summarizes $\Delta\alpha$ for Runs A–C, and Fig. 5(a) plots these results as a function of D_K . The results for Runs A–C seem to collapse respectively onto three linear functions having the same slope but with slightly different intercepts on the horizontal axis.

From the theory (10) and assumption (27), α is expected to approach zero for smaller D_K . Based on this expectation, we shift the results in Fig. 5(a) so that their fitting lines cross the origin. For

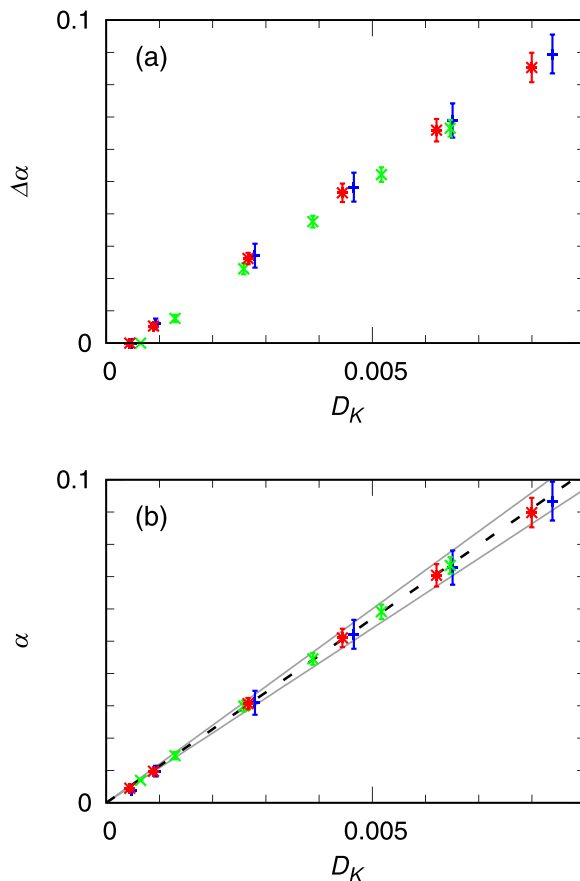


FIG. 5. (a) Slope deviation $\Delta\alpha$ as function of D_K for Runs A1–A6 (blue pluses, from left to right), Runs B1–B6 (green crosses), and Runs C1–C6 (red asterisks). The spectra for Runs A1, B1, and C1 are used as the reference spectra for Runs A, B, and C, respectively. Error bars indicate the errors in $\Delta\alpha$ shown in Table III (fifth column). (b) Same as (a) but for α (see the text for details). Dashed line is $\alpha = (2C_B)D_K$, where $C_B = 5.7$. Two gray lines in the panel indicate $\alpha = (2C_B^\pm)D_K$ with $C_B^+ = 6.0$ and $C_B^- = 5.4$, respectively.

example, we fit the results of Run C in Fig. 5(a) with a linear function $\Delta\alpha = p_C D_K + q_C$, and subtract q_C from all $\Delta\alpha$ values of Run C. We assume that $\alpha = \Delta\alpha - q_C$ for Run C. In a similar manner, we obtain α from $\Delta\alpha$ for Runs A and B. The results are summarized in Fig. 5(b). The dashed line in the panel shows $\alpha = (2C_B)D_K$ with $C_B = 5.7$, onto which all results collapse very well. Based on the errors in $\Delta\alpha$, the error in C_B is estimated approximately as $C_B = 5.7 \pm 0.3$, and two gray lines in the panel indicate $\alpha = (2C_B^\pm)D_K$ with $C_B^+ = 6.0$ and $C_B^- = 5.4$, respectively. The estimated value $C_B = 5.7 \pm 0.3$ is consistent with the Batchelor constant $C_B = 5.9 \pm 0.3$, which is directly estimated from the scalar variance spectra shown later in Fig. 6, and is also consistent with the estimations from the previous studies [15,17,21,39] obtained by large-scale DNSs of passive scalar turbulence. This agreement is as predicted from the theoretical argument by GSW21.

Figure 5 demonstrates that the simulation results are consistent with the theory (10) (where (27) is assumed to be valid) and that the present system (3), (5), and (6) converges, in the limit of $D_K \rightarrow 0$, to the passive scalar turbulence at $Sc = \infty$. Figure 5(b) also indicates that α is smaller than 0.01 for runs with the smallest D_K values (Runs A1, B1, and C1), which means that the deviation of the slope from the Batchelor spectrum due to the relaxation term is less than 1%. Therefore, we assume that

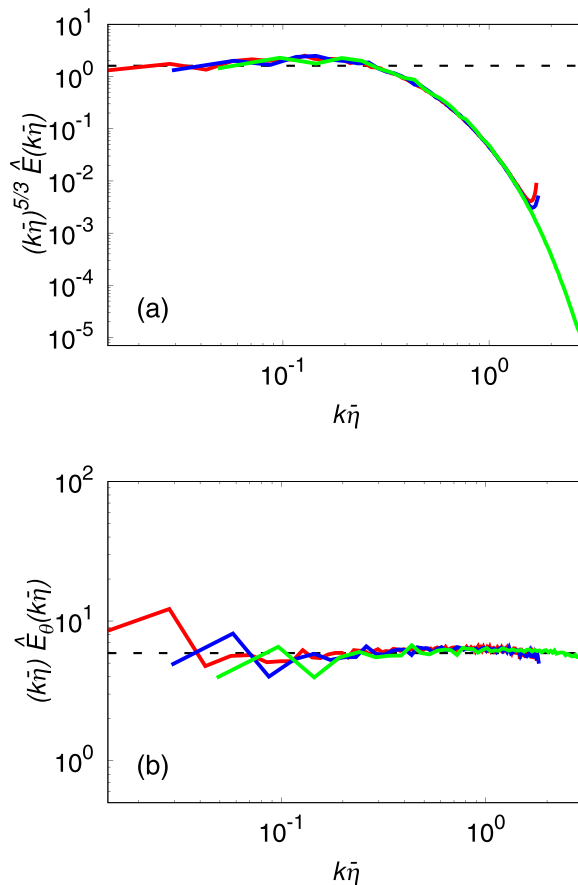


FIG. 6. (a) Mean kinetic energy spectrum normalized by Kolmogorov units and compensated by $(k\bar{\eta})^{-5/3}$. The dashed horizontal line indicates the Kolmogorov constant $C_K = 1.61$ [40]. The spectra for Runs A1, B1, and C1 are shown by blue, green, and red curves, respectively. (b) Mean scalar variance spectrum normalized based on KOC theory and compensated by $(k\bar{\eta})^{-1}$. Colors are same as in panel (a). The dashed horizontal line indicates the Batchelor constant $C_B = 5.9$.

these runs effectively correspond to the case for $\alpha = 0$, and examine various turbulence statistics for them in the following section.

C. Turbulence statistics

Figures 6(a) and 6(b) show the compensated spectra of turbulent kinetic energy, $E(k)$, and scalar variance, $E_\theta(k)$, respectively. In each panel in Fig. 6, all results collapse well onto a single curve. Because R_λ is not large enough for the present simulation, $E(k)$ does not show a clear inertial subrange with a slope of $-5/3$. The bottleneck effect is observed around $k\bar{\eta} \sim 0.1$, and $E(k)$ rapidly decreases for higher wave numbers in the dissipation range. In contrast, $E_\theta(k)$ shows a clear viscous-convective subrange with a slope close to -1 . Run B1 (green) has smaller R_λ and higher resolution in $E(k)$ than Run A1 (blue), and the result for Run B1 looks as if that for Run A1 is just shifted to the right. This indicates that the viscous-convective subrange extends further to higher wave numbers. From Fig. 6(b), the Batchelor constant is estimated approximately as $C_B = 5.9 \pm 0.3$.

From Eqs. (3) and (9), the transfer functions for the kinetic energy and the scalar variance are respectively defined by

$$\left(\frac{\partial}{\partial t} + 2\nu k^2\right)E(k, t) = T(k, t) + F(k, t), \quad (29)$$

$$\left(\frac{\partial}{\partial t} + 2\tau_\theta^{-1}\right)E_\theta(k, t) = T_\theta(k, t) + F_\theta(k, t), \quad (30)$$

where $F(k, t)$ and $F_\theta(k, t)$ are the spectra for the force and scalar injection, respectively. The transfer fluxes for the kinetic energy and the scalar variance across the wave number k are defined by

$$\Pi(k) = -\int_0^k T(q) dq, \quad (31)$$

$$\Pi_\theta(k) = -\int_0^k T_\theta(q) dq. \quad (32)$$

Note the difference in the integration range as compared to the usual definition of the transfer flux [i.e., $\Pi(k) = \int_k^\infty T(q) dq$], which gives the same results as ours because $\int_0^\infty T(q) dq = 0$. The purpose of our definitions is to avoid the influence of the error due to the effects of filtering and shot noise in the particle field. Because the error is most significant near the cutoff wave number, $\Pi_\theta(k)$ would be contaminated throughout all wave numbers if we used the definition $\Pi_\theta(k) = \int_k^\infty T_\theta(q) dq$.

Figure 7(a) shows the normalized $\Pi(k)$. The constant flux range corresponding to the inertial subrange is not seen due to small R_λ . However, the normalized $\Pi_\theta(k)$ in Fig. 7(b) (solid curves) demonstrates the constant flux range, which confirms the establishment of the viscous-convective subrange in $E_\theta(k)$. Dashed curves in the panel are the scalar transfer fluxes before removing the filtering effect. The filtering effect can be clearly seen near the cutoff wave numbers, and is reflected as an apparent loss of fluctuation energy and a decrease of the transfer flux. Because this unphysical decrease is almost removed and the constant flux range is restored, the procedure described in Eq. (25) works successfully despite its simplicity.

Figure 8(a) shows the normalized third-order structure function for the velocity field, $-\langle[\delta u(r)]^3\rangle/(\bar{\epsilon}r)$, where $\delta u(r)$ is the longitudinal velocity increment over a distance r . The dashed horizontal line in the panel indicates the Kolmogorov 4/5 law. Each result is close to r^2 for smaller r , as expected in the dissipation range. Again, due to small R_λ , the 4/5 law is not realized even for Run C1 with the largest R_λ value. Figure 8(b) (solid curves) shows the normalized third-order mixed velocity-scalar structure function, $-\langle\delta u(r)[\delta\theta(r)]^2\rangle/(\bar{\chi}r)$, where $\delta\theta(r)$ is the scalar increment over a distance r . The dashed horizontal line in the panel indicates the Yaglom 4/3 law. The range close to r^2 is not seen for these results, which indicates the absence of the dissipation range by the molecular diffusion term. All results, especially those for Run C1, satisfy the 4/3 law fairly well for smaller $r/\bar{\eta}$. This confirms the establishment of the viscous-convective subrange in physical space. Dashed curves in the panel are the structure functions before removing the filtering effect. Again, the procedure described in Eq. (25) works well to remove the filtering effect.

Note that the transfer flux in Fig. 7(b) and the structure function in Fig. 8(b) do not show any sign of the effect of shot noise despite the fact that we do not remove the shot noise contribution from the particle field. This is because these statistics are third-order and the shot noise contributions are canceled out without any treatment. The explanation below is for the structure function, but a similar argument applies to the transfer flux. The third-order mixed velocity-scalar structure function is calculated by

$$D_{L\theta\theta}(r) \equiv \langle\delta u(r)[\delta\theta(r)]^2\rangle = \langle[u_1(\mathbf{x} + r\mathbf{e}_1) - u_1(\mathbf{x})][\theta(\mathbf{x} + r\mathbf{e}_1) - \theta(\mathbf{x})]^2\rangle, \quad (33)$$

where $\mathbf{x} = (x_1, x_2, x_3)$ is the position vector, u_1 is the x_1 component for the velocity vector \mathbf{u} , and \mathbf{e}_1 is the unit vector for the x_1 direction. We divide θ into correlation part and the shot noise part as $\theta = \theta^c + \theta^s$ (for simplicity, we do not consider the filtering effect). Then we have $\delta\theta(r) = \delta\theta^c(r) + \delta\theta^s(r)$, where $\delta\theta^c(r)$ and $\delta\theta^s(r)$ are defined in the same way as $\delta\theta(r)$. Equation (33) can be expanded

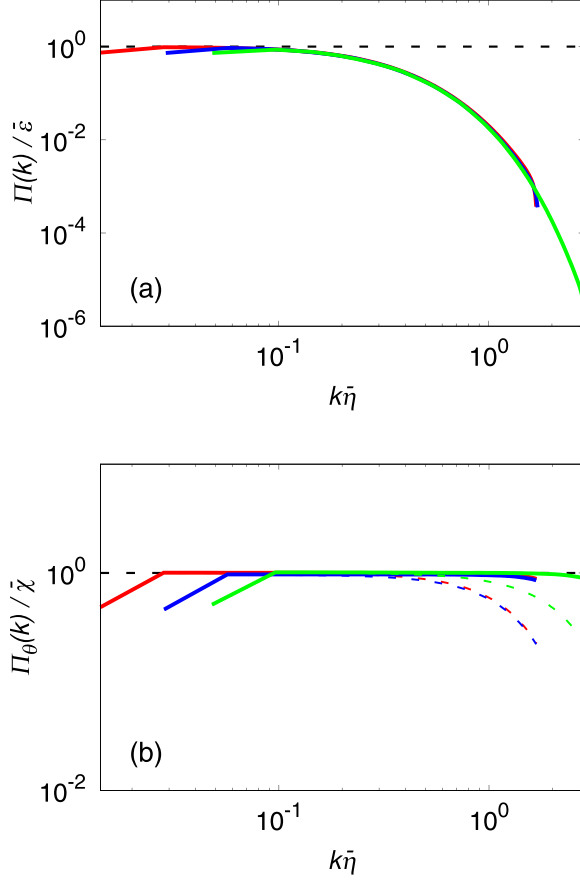


FIG. 7. Normalized transfer fluxes for (a) kinetic energy and (b) scalar variance for Runs A1 (blue), B1 (green), and C1 (red). The black dashed horizontal line in each panel indicates unity. The dashed curves in panel (b) indicate transfer fluxes including the filtering effect.

as

$$\langle \delta u(r) [\delta \theta(r)]^2 \rangle = \langle \delta u(r) [\delta \theta^c(r)]^2 \rangle + 2 \langle \delta u(r) \delta \theta^c(r) \delta \theta^s(r) \rangle + \langle \delta u(r) [\delta \theta^s(r)]^2 \rangle. \quad (34)$$

Because the shot noise part θ^s originates from a spatially uncorrelated and random distribution of particles, $\delta \theta^s$ does not correlate with others, such as $\delta \theta^c$ and δu . Then we have

$$\langle \delta u(r) \delta \theta^c(r) \delta \theta^s(r) \rangle = \langle \delta u(r) \delta \theta^c(r) \rangle \langle \delta \theta^s(r) \rangle = 0 \quad (35)$$

because $\langle \delta \theta^s(r) \rangle = 0$, and also

$$\langle \delta u(r) [\delta \theta^s(r)]^2 \rangle = \langle \delta u(r) \rangle \langle [\delta \theta^s(r)]^2 \rangle = 0 \quad (36)$$

because $\langle \delta u(r) \rangle = 0$. Therefore, the shot noise contributions are canceled out in Eq. (34), and we have $\langle \delta u(r) [\delta \theta(r)]^2 \rangle = \langle \delta u(r) [\delta \theta^c(r)]^2 \rangle$.

It is also useful to note that $\Pi_\theta(k)$ and $D_{L\theta\theta}(r)$ are related to each other as

$$\Pi_\theta(k) = -\frac{1}{2^{\frac{d}{2}+1}\Gamma(\frac{d}{2})} k^{1+\frac{d}{2}} \int_0^\infty dr r^{\frac{d}{2}} J_{\frac{d}{2}+1}(kr) \frac{D_{L\theta\theta}(r)}{r}, \quad (37)$$

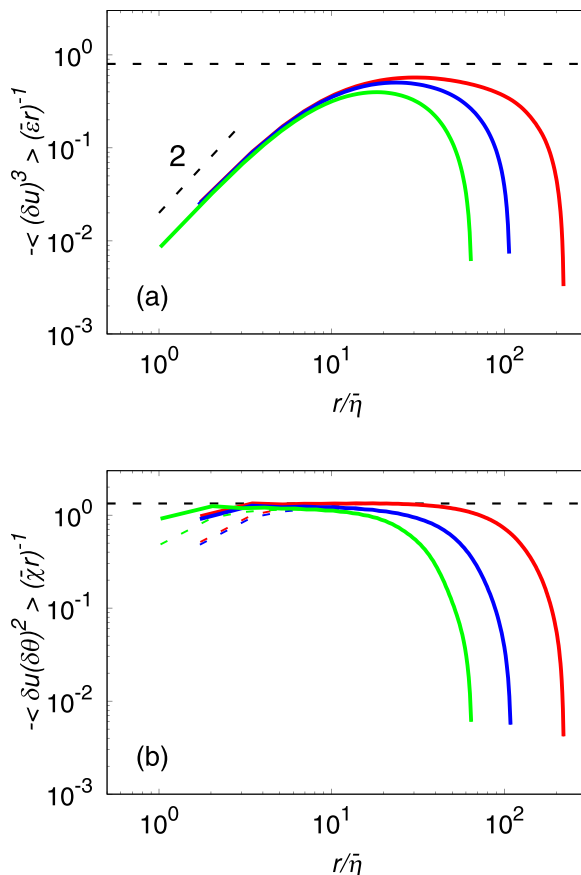


FIG. 8. (a) Normalized third-order structure function for velocity field. The dashed horizontal line indicates $4/5$. The short dashed line labeled “2” is proportional to r^2 . (b) Normalized third-order mixed velocity-scalar structure function. The dashed horizontal line indicates $4/3$. Colors are for Runs A1 (blue), B1 (green), and C1 (red). The dashed curves in panel (b) indicate the structure functions including the filtering effect.

and

$$D_{L\theta\theta}(r) = -2^{\frac{d}{2}+1} \Gamma\left(\frac{d}{2}\right) r^{2-\frac{d}{2}} \int_0^\infty dk k^{-\frac{d}{2}} J_{\frac{d}{2}+1}(kr) \Pi_\theta(k), \quad (38)$$

where d is the space dimension, $J_{\frac{d}{2}+1}(x)$ is the Bessel function of the order $d/2 + 1$, $\Gamma(x)$ is the Γ function. When $d = 3$ and $\bar{\Pi}_\theta = \chi$, we have $D_{L\theta\theta}(r) = -(4/3)\chi r$ and vice versa [41]. These expression is convenient because the scalar field is first computed on the grid points by the interpolation in the present method and so is for the $D_{L\theta\theta}(r)$. Then $\Pi_\theta(k)$ is directly computed in terms of Eq. (37) without transforming the scalar field to that in the wave-number space.

Figure 9 compares the scalar transfer flux calculated from $D_{L\theta\theta}(r)$ for Run C1 based on the relationship (37) (blue curve) with the transfer flux calculated in the usual way (red curve). The overall agreement is good, especially for the middle wave-number range $0.05 < k\bar{\eta} < 1$. The underestimate and oscillation of the blue curve near the lowest and highest wave numbers are due to relatively slow convergence of the integral including the Bessel function.

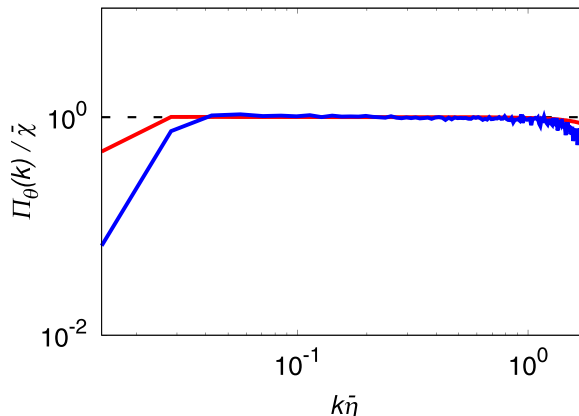


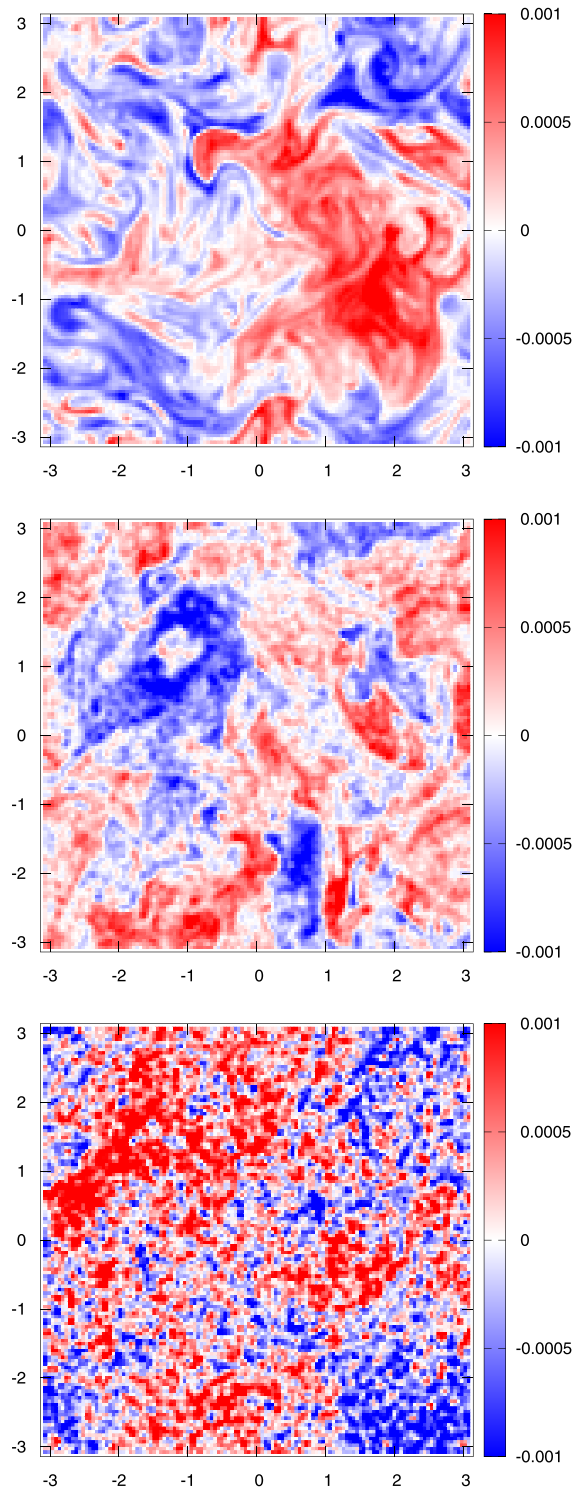
FIG. 9. Normalized transfer flux for scalar variance calculated from the third-order mixed velocity-scalar structure function $D_{L\theta\theta}(r)$ for Run C1 based on the relationship (37) (blue). Red curve is the transfer flux calculated in the usual way [same as the red curve in Fig. 7(b)].

D. Visualization

We now examine the results of visualization. Figure 10 shows snapshots of 2D slices of the particle field for Runs D1–D3 in the statistically steady state. Note that the figure shows $\tilde{\theta}$, which includes the effects of filtering and shot noise. The number of particles per grid cell is 512, 32, and 2 for Runs D1, D2, and D3, respectively (Table I), and this difference in number density clearly affects the visualization results. For Run D1 (top panel), the scalar distribution is so smooth that it is almost indistinguishable from a continuous scalar field. The distribution also shows typical features of passive scalar turbulence: large-scale regions with relatively large negative and positive values (plateaus) separated by sharp fronts with an abrupt change of the scalar value [25,42,43]. For Run D2 (middle panel), large-scale structures of the particle field are still visible but the smoothness of the distribution is lost. Many small dots with positive and negative values exist in the background due to shot noise. For Run D3 (bottom panel), the scalar distribution is significantly contaminated by shot noise and we can just barely see the large-scale structure of wave number 2 that originates from the external scalar source.

Figure 11 shows the raw results for the variance spectrum of the particle field for Runs D1–D3 [$E_{\tilde{\theta}}(k)$ in Eq. (21), which includes the effects of filtering and shot noise]. As shown in Eq. (23), the relative contribution of shot noise is inversely proportional to the mean particle number density n_0 . For the spectrum of Run D1 (red curve), n_0 is sufficiently large that the shot noise cannot be seen in the spectrum, which corresponds to the smooth distribution shown in Fig. 10(a). For Run D2 (blue curve in Fig. 11), the shot noise appears for larger wave numbers ($k' > 10$), which corresponds to the distribution with many small dots in Fig. 10(b). For Run D3 (green curve in Fig. 11), the maximum value of the shot noise near the cutoff wave number is comparable to the amplitude of the spectrum around $k' = 3$. Accordingly, the spatial structure of the particle field is not visible except for the largest scales affected by the external source.

Figure 12 shows snapshots of the time evolution of the flow field (cyan, isosurface of $|\nabla \times \mathbf{u}|^2$) and the particle field (yellow, isosurface of $\tilde{\theta}$) for Run D1. Here, the effect of the relaxation term in Eq. (6) can be neglected because the elapsed time for these three panels is 0.02 and is much shorter than the relaxation time ($\tau_{\theta} = 100$, Table I). The figure exhibits typical features of passive scalar turbulence. From Fig. 12(a), we can see a sheetlike structure of the scalar field (pink circle) that corresponds to the scalar front. Below this sheetlike structure, a vortex tube (marked by a thick red arrow) extends from the front to back of the panel. This vortex tube rotates clockwise, and as time elapses [from Figs. 12(a) to 12(c)], it rolls up the sheetlike structure.

FIG. 10. Snapshots of particle field $\tilde{\theta}$ for Runs D1 (top), D2 (middle), and D3 (bottom).

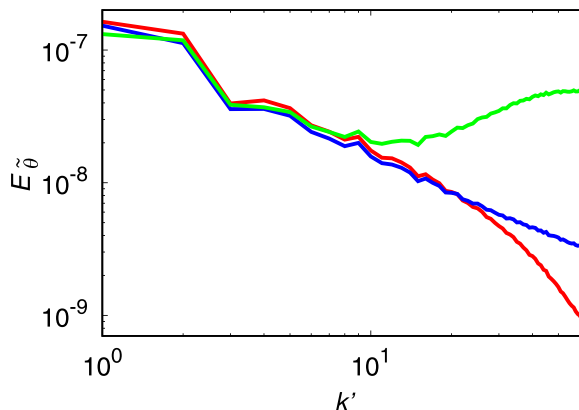


FIG. 11. Mean scalar variance spectra $E_{\theta}(k)$ [including the effects of filtering and shot noise, see (21)]. Lines are for Runs D1 (red), D2 (blue), and D3 (green).

E. On resolution of particle field

Before closing this section, we note on resolution of the particle field. In the present simulation, particles distribute almost homogeneously and randomly in the domain. The average distance of particles can be estimated as $\Delta x_p = n_0^{-1/3}$. Table I (the last column) summarizes Δx_p for the present simulation.

In the spectral space, the scalar variance spectrum begins to be contaminated by the shot noise at wave numbers higher than $k'_p = (\pi/\Delta x_p) \approx (C_B/2\pi)VD_K n_0$ which is obtained by equating $E_{\theta}(k') \propto k'^{-1}$ to k'^2 spectrum. In fact, $k'_p \approx 60$ for C1 and 15 for D3, respectively, which is consistent with the red curve in Fig. 2 and the green curve in Fig. 11 and the visualization in Fig. 10. When $k'_{\max} < k'_p$, the contamination by the shot noise does not appear. For length scales smaller than Δx_p , the expected value of the particle number is less than 1, therefore, the average over large ensemble is necessary to extract the statistics for the correlated particle distribution at scales below Δx_p . This is the reason why the long time average is necessary to obtain the coherent scalar spectrum at large wave numbers. It should be noted that the coherent spectrum is obtained after the shot noise spectrum is subtracted, but the same procedure can not be applied to extract the spatial structure of the particle field $\theta(x, t)$ at instant time for the scales below Δx_p . By increasing the number density, we can make Δx_p smaller and see the structure of θ for even smaller scales. When n_0 becomes large, the computational costs increases, but the rate of increase is milder than in the case of the conventional Eulerian computation. In this respect, the present method may be regarded as an alternative way which replaces the huge computational resource for space by large number of particles and long time integration with smaller grid points for the velocity.

VI. LARGE-SCALE SIMULATIONS

Given the results for the variance spectra in Fig. 6(b), the next question that naturally arises is whether we will obtain $k^{-5/3}$ (corresponding to the Obukhov-Corrsin spectrum) in the smaller wave-number range if we further increase the Reynolds number. To answer this question, we conducted large-scale simulations (Runs E and F), where the number of grid points and the Reynolds number are expanded to $N_{\text{grid}} = 1024^3$ and $R_{\lambda} = 330$ for Run E, and $N_{\text{grid}} = 2048^3$ and $R_{\lambda} = 550$ for Run F, while the parameters such as the resolution ($k_{\max}\bar{\eta}$), τ_{θ} , and D_K are similar to those for Run C1 (See Table I–III).

Figures 13(a) and 13(b) show the spectra $E(k)$ and $E_{\theta}(k)$, respectively. Now, $E(k)$ shows a clear inertial subrange with a slope of $-5/3$ to the left of the bottleneck ($k\bar{\eta} < 0.04$). $E_{\theta}(k)$ also shows a $k^{-5/3}$ range in the smaller wave numbers, where the spectra agree well with the Obukhov-Corrsin

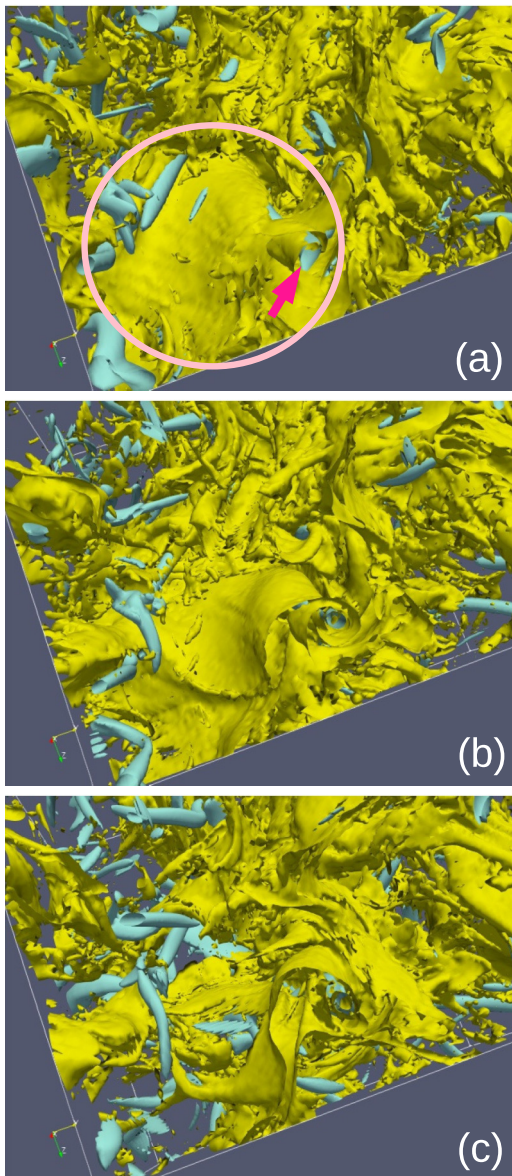


FIG. 12. Snapshots of time evolution for Run D1. Cyan and yellow indicate the contour surfaces of $|\nabla \times \mathbf{u}|^2$ and $\bar{\theta}$, respectively. Panels (b) and (c) are 0.01 and 0.02 nondimensional time units after panel (a), respectively. In panel (a), the pink circle indicates the position of the sheetlike structure of the particle field $\bar{\theta}$, and the red arrow indicates the position of a vortex tube.

spectrum multiplied by $k\bar{\eta}$ with the nondimensional constant $C_{OC} = 0.68$ (dashed oblique line in the panel). The transition wave number from $k^{-5/3}$ to k^{-1} is estimated approximately as $k_*\bar{\eta} \sim 0.04$, which is consistent with 0.036 reported in the DNS [26] and 0.03 reported by the laboratory experiment [8]. Interestingly, the transition wave number $k_*\bar{\eta} \sim 0.04$ seems to coincide with the transition wave number from $k^{-5/3}$ to the bottleneck in $E(k)$ in Fig. 13(a).

Figures 14(a) and 14(b) show the transfer fluxes $\Pi(k)$ and $\Pi_\theta(k)$, respectively. $\Pi(k)$ is constant for $k\bar{\eta} < 0.04$, which corresponds to the range with $E(k) \propto k^{-5/3}$ in Fig. 13(a). $\Pi_\theta(k)$ is constant

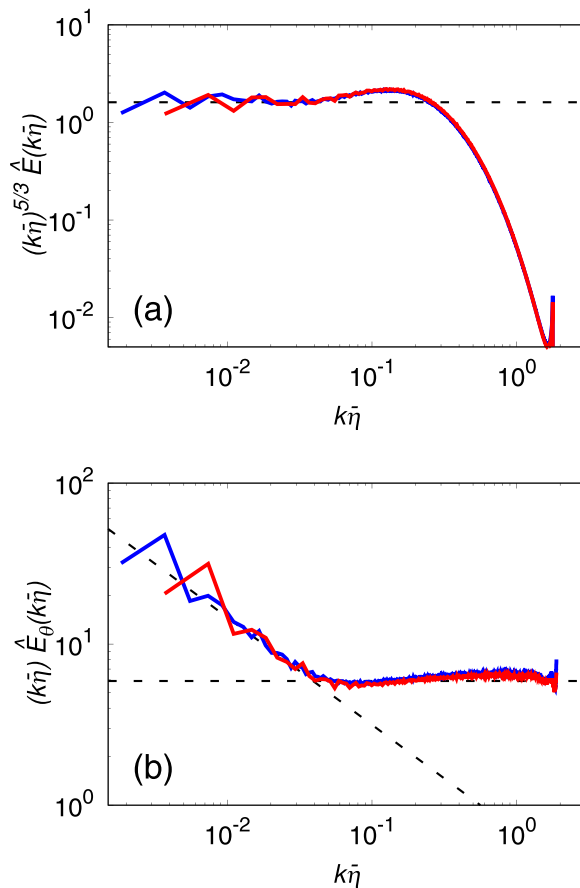


FIG. 13. Same as Fig. 6 but for Runs E (red) and F (blue). The dashed oblique line indicates the Obkhov-Corsin spectrum multiplied by $k\bar{\eta}$ with a nondimensional constant $C_{OC} = 0.68$.

for the entire wave-number range (except near the smallest and largest wave numbers), irrespective of the slope of $E_\theta(k)$ in Fig. 13(b). This result is as predicted by turbulence theory. Figure 15 shows $D_{L\theta\theta}(r)$. The basic characteristics are similar to Fig. 8(b), but the structure functions in Fig. 15 agree with the Yaglom 4/3 law for wider range.

Figure 16 shows the same comparison as Fig. 9 but for Run F. The result is qualitatively similar to Fig. 9, but the two curves in Fig. 16 agree for wider wave-number range.

VII. SCALAR TRANSFER FLUX AND DISSIPATION

So far we have seen that the spectrum of the passive scalar $E_\theta(k)$ computed by the present method is consistent with that for the infinite Schmidt number. But it is natural to ask how the injected scalar fluctuations at large scales are transferred and dissipated. To answer the question, we examine the transfer flux of the scalar variance in the wave-number space. Here, we consider the case of large-scale simulations in the previous section, where Reynolds number is large and $D_L \ll 1$ (D_L is about 0.02 and 0.03 for Runs E and F, respectively).

Integrating Eq. (30) from k_L to k and using Eq. (32), we obtain

$$\frac{\partial G(k, t)}{\partial t} = -\frac{2}{\tau_\theta} G(k, t) - \Pi_\theta(k, t) + \chi_{in}(t), \quad (39)$$

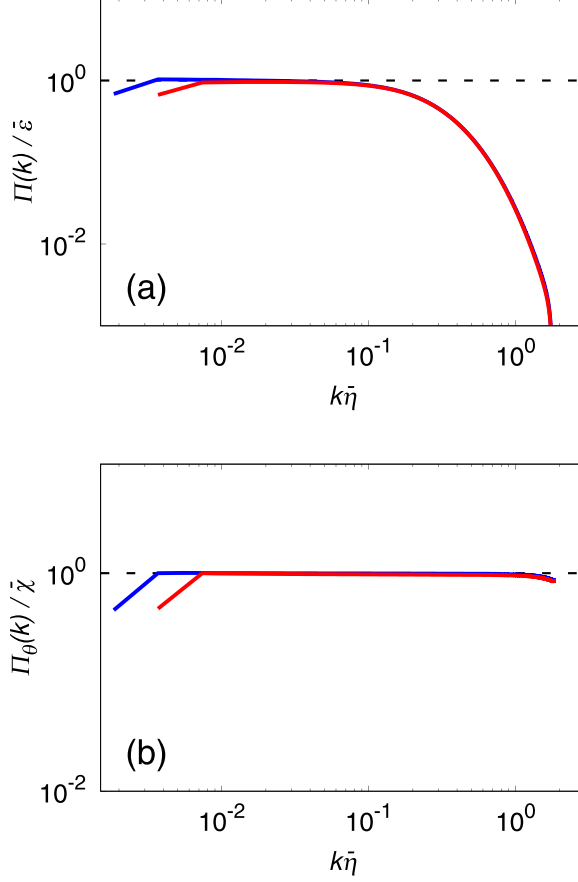


FIG. 14. Same as described in the caption of Fig. 7 but for Runs E (red) and F (blue).

where $G(k, t)$ is defined by

$$G(k, t) = \int_{k_L}^k E_\theta(q, t) dq, \quad (40)$$

and χ_{in} is the rate of the scalar fluctuation injection

$$\chi_{\text{in}}(t) = \int_{k_L}^k F_\theta(q, t) dq. \quad (41)$$

Note that the scalar injection $F_\theta(k, t)$ spectrum has the spectral support at low wave-number band, and this band is assumed to be included in the integration range $k_L \leq q \leq k$. In the arguments to follow, we tentatively assume that statistically steady state is established under the finite scalar dissipation due to the relaxation term, and will examine later whether the obtained results are consistent with the assumption made here.

Suppose that the scalar spectrum has two scaling ranges as in Eq. (14). Substituting the power-law spectrum into the first term of the right-hand side of Eq. (39) and noting that the eddy turnover time in the inertial convective range is $\tau(k) = \bar{\epsilon}^{-1/3} k^{-2/3}$ and that $\tau(k_L) = T$ is the large-eddy turnover

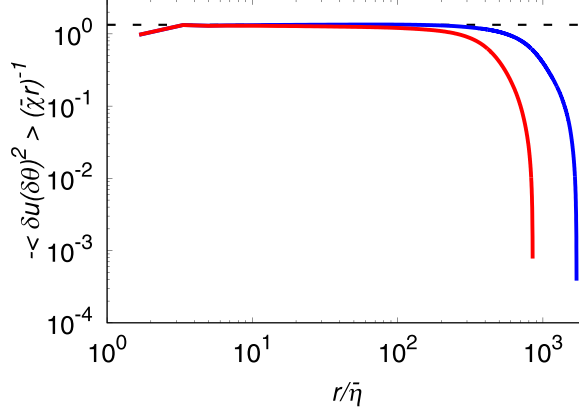


FIG. 15. Same as described in the caption of Fig. 8(b) but for Runs E (red) and F (blue).

time, we obtain for $k_L \ll k \ll k_d$

$$\frac{2}{\tau_\theta} G(k) = 3C_{OC} \bar{\chi}_{in} \left[1 - \left(\frac{k}{k_L} \right)^{-2/3} \right] D_L, \quad (42)$$

and for $k_L \ll k_d \ll k$

$$\frac{2}{\tau_\theta} G(k) = 3C_{OC} \bar{\chi}_{in} \left[1 - \left(\frac{k_d}{k_L} \right)^{-2/3} \right] D_L + \bar{\chi}_{in} \left[1 - \left(\frac{k}{k_d} \right)^{-\alpha} \right]. \quad (43)$$

We first consider the inertial convective range $k_L \ll k \ll k_d$. From Eq. (42), the term $\frac{2}{\tau_\theta} G(k)$ is much smaller than $\bar{\chi}_{in}$ since $D_L \ll 1$, and is negligible in Eq. (39). Therefore in the inertial convective range, the scalar variance injected at the rate of $\bar{\chi}_{in}$ by the external source is transferred through this range without loss and thus

$$\Pi_\theta(k) = \bar{\chi}_{in}, \quad (44)$$

which is consistent with the idea of the constant scalar transfer rate throughout this range.

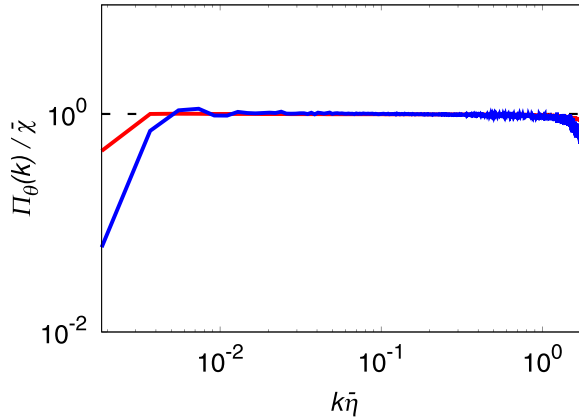


FIG. 16. Normalized transfer flux for scalar variance calculated from the third-order mixed velocity-scalar structure function $D_{L,\theta\theta}(r)$ for Run F based on the relationship (37) (blue). Red curve is the transfer flux calculated in the usual way [same as the blue curve in Fig. 14(b)].

Now consider the viscous-convective range $k \gg k_d$. The first term in the right-hand side of Eq. (43) is again negligible since $D_L \ll 1$ and, from Eqs. (43) and (39), the transfer flux is

$$\Pi_\theta(k) = \bar{\chi}_{\text{in}} - \bar{\chi}_{\text{in}} f_p\left(\frac{k}{k_d}\right), \quad f_p(x) = 1 - x^{-\alpha}. \quad (45)$$

For very small but finite $\alpha > 0$, and for wave numbers k near k_d ($k \gtrsim k_d$), the factor $f_p(k/k_d)$ vanishes. Again we have

$$\Pi_\theta(k) = \bar{\chi}_{\text{in}}. \quad (46)$$

However, at large $k \gg k_d$, $f_p(k/k_d)$ tends to unity, so that the second term $\bar{\chi}_{\text{in}} f_p(k/k_d)$ becomes comparable to the first term $\bar{\chi}_{\text{in}}$ in Eq. (45) as $\frac{2}{\tau_\theta} G(k) \rightarrow \bar{\chi}_{\text{in}}$ and thus

$$\Pi_\theta(k) = \bar{\chi}_{\text{in}} - \frac{2}{\tau_\theta} G(k) \rightarrow 0. \quad (47)$$

The damping due to the relaxation becomes finite and balances the transfer flux which is coming through the viscous-convective range, and $\Pi_\theta(k)$ vanishes.

It is, however, important to understand how large wave number is necessary for $f_p(x)$ to approach unity. In the standard numerical computation, the maximum integer in the computer is about $2^{31} \approx 10^9$, which means that the maximum wave number (integer) is $k'_{\text{max}} = 10^9$. However, k'_d is about 512 in the DNS with $N = 2048^3$ grid points, so that $(k'_{\text{max}}/k'_d) \approx 10^6$. However, $\alpha = (2C_B)D_K \approx 5 \times 10^{-3}$ in the present DNSs, and thus $f_p(k/k_d) = 1 - (k'_{\text{max}}/k'_d)^{-\alpha} \approx [1 - (10^6)^{-0.005}] \approx 0.07$, only 7% of the total flux is dissipated by this term even for DNS using $(10^9)^3$ grid points. This means that the dissipation due to the relaxation term is effectively zero in the Eulerian sense and therefore $\Pi_\theta = \bar{\chi}_{\text{in}}$ in the spectral space of $k' < k'_{\text{max}}$ in the present computation. In the actual computation of the spectrum, the scalar fluctuations at scales below Δx ($k' > k'_{\text{max}}$) are distributed onto the surrounding grid points with the linear weight, which is effectively a coarse graining, thus most of scalar fluctuation beyond k'_{max} is cut off by the filter $F_{\text{filter}}(k)$ as seen in Fig. 1 and in Appendix C.

It is very essential and important to understand that in the present study the decay or growth of the amount of scalar carried by each particle is computed in the Lagrangian frame, not in the Eulerian frame. The scalar of each particle which is passively advected by turbulent flow is computed according to Eq. (6), not to the Eulerian equation (9). Actually, the total dissipation due to the relaxation is computed by Eq. (19) by summing up the square of the scalar fluctuations over all particles, and indeed balances perfectly with the total scalar injection as $\bar{\chi}_{\text{in}} = \bar{\chi}$ to establish the statistically steady state.

It is useful to compare the above analysis with the usual case of the diffusion term $2\kappa k^2 E_\theta(k)$ with very small diffusivity (or very high Schmidt number). As before, we assume that the scalar spectrum $E_\theta(k)$ at high Schmidt number is, in the steady state,

$$E_\theta(k) = \begin{cases} C_{\text{OC}} \bar{\chi}_{\text{in}} \bar{\epsilon}^{-1/3} k^{-5/3} & \text{for } k \ll k_d, \\ C_B \bar{\chi}_{\text{in}} (\bar{\epsilon}/\nu)^{-1/2} k^{-1} (1 + \gamma(k/k_B)) \exp(-\gamma(k/k_B)) & \text{for } k \gg k_d, \end{cases} \quad (48)$$

$$k_B = \sqrt{\text{Sc}} k_d, \quad \gamma^2 = 6C_B. \quad (49)$$

Although there are arguments about the spectral form in the far diffusive range, whether or not exponential or Gaussianly decaying, only the rapid decay in the diffusive range is sufficient for the arguments to follow, and we use the exponential decay for simplicity [3,9,10,14,21]. Substituting Eq. (48) into the accumulated dissipation integral, we obtain for $k_L \ll k_d \ll k$

$$\begin{aligned} D_m(k) &= \int_{k_L}^k 2\kappa q^2 E_\theta(q) dq \\ &= \frac{3}{2} C_{\text{OC}} \bar{\chi}_{\text{in}} \text{Sc}^{-1} \left[1 - \left(\frac{k_L}{k_d}\right)^{4/3} \right] + \bar{\chi}_{\text{in}} \left[1 - \left(1 + \gamma \frac{k}{k_B} + \frac{1}{3} \gamma^2 \left(\frac{k}{k_B}\right)^2 \right) e^{-\gamma(k/k_B)} \right] \end{aligned}$$

$$\approx \bar{\chi}_{\text{in}} f_d \left(\frac{k}{k_B} \right),$$

$$f_d(x) = 1 - e^{-\gamma x} \left(1 + \gamma x + \frac{1}{3} \gamma^2 x^2 \right), \quad (50)$$

since $\text{Sc} \gg 1$. A common feature of Eqs. (43) and (50) is the fact that the dissipation of the scalar variance is achieved in the viscous-convective range. However, the difference is in the speed of accumulation of the dissipation. The former is very slow and the convergence to $\bar{\chi}_{\text{in}}$ is achieved at infinite wave number, while the latter is $2C_B(k/k_B)^2 = 2C_B(k/k_d)\text{Sc}^{-1}$ for small k/k_B and has the exponential cut off at k_B . It is this difference that the present method allows us to successfully compute the scalar spectrum close to $E_\theta(k) \propto k^{-1}$ for small D_K . It is interesting and important to see that the transition of the exponent from $-5/3$ to $-1 - \alpha$ occurs at around $k_* \eta \approx 0.04$ which is much smaller than the condition $k\eta \gg 1$ in the theory for the viscous-convective range. So far we have no explanation for this observation, but the approximation of the uniform velocity gradient for the convective term of the scalar [$T_\theta(k) \approx (\bar{\epsilon}/\nu)^{1/2} \partial E_\theta(k)/\partial k$ as used in the Batchelor theory] is effective to some extent for the range $k_* < k < k_d$, in which the transition from $-5/3$ to $-1 - \alpha$ occurs gradually. We infer that this gradual transition appears as slight increase of the compensated spectrum $kE_\theta(k)$ over the range $0.1 < k\eta < 1$ and the horizontal curves are seen for $k\eta > 1$ where the theory works. Search for further explanation is the future work.

VIII. SUMMARY AND DISCUSSION

In the present study, we extended the previous study by Ref. [26] and conducted a more careful and comprehensive investigation of the simulation method which uses a fully Lagrangian description of scalar carried by particle to study passive scalar turbulence at high Schmidt and Reynolds numbers. We considered fluid particles with scalar properties (θ_{pj}) and examined statistical properties of the particle field θ , which is the spatial distribution of θ_{pj} . The scalar θ_{pj} for each particle is relaxed with a relaxation time τ_θ and is affected by the field f_θ , and these processes play the roles of dissipation and the external source for the fluctuation of the particle field θ . The evolution equation for θ in the Eulerian frame is the advection-diffusion equation for a passive scalar except that the molecular diffusion term ($\kappa \nabla^2 \theta$) is replaced by the relaxation term ($-\theta/\tau_\theta$). The theoretical analysis in [26] predicts that, as the parameter D_K in Eq. (12) decreases and the effect of the relaxation term becomes smaller, the scalar variance spectrum $E_\theta(k)$ converges to the Batchelor spectrum with an infinite Schmidt number.

We conducted parameter sweep simulations with a relatively moderate number of particles and grid points (less than 256^3). After carefully removing the effects of filtering and shot noise, we investigated the variance spectrum of the particle field and showed that, with the assumption (27), the slope of the compensated spectrum is given by $\alpha = (2C_B)D_K$ as expected from the theory, and C_B is estimated as $C_B = 5.7 \pm 0.3$. This value of C_B is consistent with the Batchelor constant C_B reported in previous DNS studies [15,17,21,39], which supports the validity of the present simulation.

Because α is estimated to be smaller than 0.01 for runs with the smallest D_K (Runs A1, B1, and C1), we assumed that the spectra modification due to the relaxation term for these runs is negligible. We investigated turbulence statistics for these runs and confirmed their consistency with turbulence theory, such as the constancy of the transfer flux and the Yaglom 4/3 law. For runs with a sufficiently large particle number density, the visualized particle field is almost indistinguishable from a continuous scalar field and shows features commonly seen in passive scalar turbulence, such as plateaus, fronts, and sheetlike structures.

We also conducted large-scale simulations with Reynolds numbers up to $R_\lambda = 550$ and showed that the scalar variance spectrum has the slope -1 and $-5/3$ for higher and lower wave numbers, respectively. The Batchelor and Obkhov-Corrsin constants are estimated to be consistent with the

previous DNS studies, and the transition wave number between the two slopes is found to be about $k_*\eta \sim 0.04$.

In addition, we theoretically discussed how the injected scalar fluctuations at large scales are transferred and dissipated in the present simulation. It was shown that, if an Eulerian method with the standard spectral method would be used for the scalar equation, even the largest possible simulation with $(k'_{\max}/k'_d) \approx 10^6$ could dissipate only a tiny amount of scalar fluctuation energy in the wave-number range $k' < k'_{\max}$, contrasting the advantage of the present method where the Lagrangian frame is used for the scalar equation and the balance between the injection and dissipation for the scalar fluctuations is established.

One important task for future research is to investigate the scalar structure function exponent for higher orders. Iyer *et al.* (2018) [44] showed by DNSs of scalar turbulence at $R_\lambda = 650$ and $Sc = 1$ that the scaling exponents for the scalar structure function saturate for higher order moments (beyond about 12). They also conjectured that this saturation may be enhanced by the weak diffusion for $Sc \gg 1$, which was later confirmed by Ref. [19]. The present simulation can be validated by investigating the scalar structure function exponent and checking the consistency with these previous studies. Another important task is to examine the effects of processes such as particle momentum inertia, gravity, and condensation-evaporation. Based on observations at the German Alps [45,46], it has been reported that there are turbulence-induced voids inside natural clouds [47]. It is important to investigate how such phenomenon can affect the scalar variance spectrum and other statistics.

We note that the present simulation has room for improvement. For example, we used linear interpolation to estimate the fluid velocity at each particle position from the surrounding grid points, but previous studies [48,49] recommended cubic splines for calculation of particle trajectories in turbulence. Because the resolution in the present study is $k_{\max}\bar{\eta} > 1.6$ (Table II), the smallest scales in the turbulent velocity field are resolved well, and therefore we expect that a simple linear-interpolation scheme still works. Nevertheless, the effect of a different interpolation scheme should be clarified in a future study.

ACKNOWLEDGMENTS

We would like to thank two anonymous reviewers for helpful comments. We are also grateful to Mister Kei Nakajima for his technical support. The present study was supported by the Japan Ministry of Education, Culture, Sports, Science and Technology (KAKENHI Grants No. 20H00225 and No. 20H02066) and the Japan Society for the Promotion of Science (KAKENHI Grant No. 18K03925). The present research used the supercomputer FUGAKU provided by the RIKEN Center for Computational Science through the HPCI System Research project (projects hp210056, hp220054, and hp240059), and the plasma simulator ‘‘Raijin’’ provided by the National Institute for Fusion Science through the NIFS Collaboration Research Program (NIFS22KISS002, NIFS23KISS033). The computational support provided by the Japan High Performance Computing and Networking plus Large-scale Data Analyzing and Information Systems (jh220003, jh230019, and jh240020), and High Performance Computing (HPC2022, HPC2023, and HPC2024) at Nagoya University is also gratefully acknowledged.

APPENDIX A: DEFINITIONS OF TURBULENCE PARAMETERS

The kinetic energy is defined by

$$\frac{1}{2}\langle u_i^2 \rangle = \int_0^\infty E(k)dk, \quad (\text{A1})$$

where u_i ($i = 1, 2, 3$) are components of velocity vector \mathbf{u} (repeated indices are summed), $E(k)$ is the kinetic energy spectrum, and the angle brackets $\langle \dots \rangle$ represent the ensemble average. (Note that we approximated the ensemble average by spatial and temporal averages to estimate turbulence

parameters in numerical simulations.) The mean energy dissipation rate is defined by

$$\bar{\epsilon} = \frac{\nu}{2} \langle (\partial_i u_j + \partial_j u_i)^2 \rangle. \quad (\text{A2})$$

The integral scale, Taylor microscale, and Kolmogorov scale are respectively defined by

$$\mathcal{L} = \left(\frac{3\pi}{4E} \right) \int_0^\infty k^{-1} E(k) dk, \quad (\text{A3})$$

$$\lambda = \sqrt{\langle u_1^2 \rangle / \langle (\partial_1 u_1)^2 \rangle}, \quad (\text{A4})$$

$$\bar{\eta} = (\nu^3 / \bar{\epsilon})^{1/4}. \quad (\text{A5})$$

The large-eddy turnover time and Kolmogorov time are respectively defined by

$$T = \mathcal{L} / u_{\text{rms}}, \quad (\text{A6})$$

$$\tau_K = (\nu / \bar{\epsilon})^{1/2}, \quad (\text{A7})$$

where $u_{\text{rms}} = \sqrt{2E/3}$ is the rms velocity. The Taylor microscale Reynolds number is defined by

$$R_\lambda = u_{\text{rms}} \lambda / \nu. \quad (\text{A8})$$

APPENDIX B: DISSIPATION RATE OF SCALAR VARIANCE

Multiplying Eq. (9) by θ and using the nondivergent condition, we obtain

$$\frac{\partial}{\partial t} (\theta^2) + \nabla \cdot (\theta^2 \mathbf{u}) = -\frac{2}{\tau_\theta} \theta^2 + 2\theta f_\theta, \quad (\text{B1})$$

in the Eulerian representation. Assuming that the statistics are homogeneous and isotropic and that the scalar force f_θ is Gaussian white, we take an ensemble average of the above equation and have

$$\frac{\partial}{\partial t} (\langle \theta^2 \rangle) = -\frac{2}{\tau_\theta} \langle \theta^2 \rangle. \quad (\text{B2})$$

Thus, the dissipation rate χ of the scalar field θ is given by $2\langle \theta^2 \rangle / \tau_\theta$.

To derive the scalar variance $\langle \theta^2 \rangle$, we use a similar procedure as used for a continuous scalar field. Namely, we first calculate the two-point correlation function $\langle \theta(\mathbf{r}_1, t) \theta(\mathbf{r}_2, t) \rangle$ which can be expressed as a function of the separation $r = |\mathbf{r}_1 - \mathbf{r}_2|$, and then obtain the scalar variance by taking the limit $r \rightarrow 0$. From the definition Eq. (7), the two-point quantity $\theta(\mathbf{r}_1, t) \theta(\mathbf{r}_2, t)$ is

$$\theta(\mathbf{r}_1, t) \theta(\mathbf{r}_2, t) = \frac{1}{n_0^2} \sum_{i,j=1}^{N_p} \theta_{pi} \theta_{pj} \delta(\mathbf{r}_1 - \mathbf{x}_{pi}) \delta(\mathbf{r}_2 - \mathbf{x}_{pj}). \quad (\text{B3})$$

As described in Appendix C of Ref. [34], under the assumption that the statistics are homogeneous and isotropic, the ensemble average of the above equation is expressed as

$$\langle \theta(\mathbf{r}_1, t) \theta(\mathbf{r}_2, t) \rangle = \frac{1}{n_0} \langle \theta_{pj}^2 \rangle \delta(\mathbf{r}) + \langle \theta_{pi} \theta_{pj} \rangle \quad (i \neq j). \quad (\text{B4})$$

Here, the first term on the right-hand side is the contribution from the shot noise part and $\langle \theta_{pj}^2 \rangle$ indicates the ensemble average of the square of the particle scalar value θ_{pj} . The second term is the contribution from the correlated part and $\langle \theta_{pi} \theta_{pj} \rangle$ indicates the ensemble average of the product of the particle scalar values θ_{pi} and θ_{pj} for two particles that are separated by a distance r .

Since we need the dissipation rate for the correlated part of the scalar field θ , we should only use the term $\langle \theta_{pi} \theta_{pj} \rangle$ in Eq. (B4). In the limit $r \rightarrow 0$, we have $\theta_{pi} = \theta_{pj}$. This is because particles move in the same way as fluid particles in incompressible flow: If two particles are in the same position at

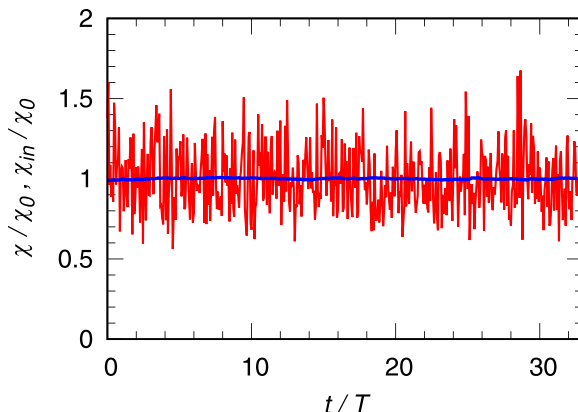


FIG. 17. Time-evolutions of the injection rate, χ_{in} (red), and the dissipation rate, χ (blue), of the scalar variance for Run C1 after the statistically steady state is attained. Both are normalized by $\chi_0 = 3.94 \times 10^{-8}$ which is the time average of χ for Run C1. The abscissa is the time t normalized by the large-eddy turnover time T for Run C.

certain time, then the trajectories of those two particles are identical and therefore scalar values for those particles (θ_{pi} and θ_{pj}) are equal as well. Thus, we obtain $\langle \theta_{pj}^2 \rangle$ for the variance of the correlated part. In the simulation, we replace the ensemble average $\langle \langle \rangle \rangle$ with the average over particles and time $\langle \langle \rangle_p \rangle$ and calculate the dissipation rate χ as follows:

$$\chi = \frac{2}{\tau_\theta} \langle \theta_p^2 \rangle_p, \quad (\text{B5})$$

where $\langle \theta_p^2 \rangle_p$ is the time average of $\sum_{j=1}^{N_p} \theta_{pj}^2 / N_p$.

Figure 17 compares the time evolutions of the injection rate, χ_{in} , and the dissipation rate, χ , of the scalar variance for Run C1 after the statistically steady state is attained. χ_{in} fluctuates significantly more than χ . Their means \pm standard deviations are $\bar{\chi}_{\text{in}} = (3.94 \pm 0.80) \times 10^{-8}$ and $\bar{\chi} = (3.94 \pm 0.02) \times 10^{-8}$, respectively, which confirms that $\bar{\chi}$ balances perfectly with $\bar{\chi}_{\text{in}}$ at the statistically steady state.

APPENDIX C: FITTING FUNCTION FOR FILTERING EFFECT

The fitting function for the filtering effect F_{filter} is given by

$$F_{\text{filter}}(\hat{k}) = \exp\left(\sum_{i=1}^{10} c_i \hat{k}^{2i}\right), \quad (\text{C1})$$

where $\hat{k} = (k'/k'_{\text{max}})$, k'_{max} is the cutoff wave number, $c_1 = -1.4985$, $c_2 = -3.6307$, $c_3 = 30.1292$, $c_4 = -113.955$, $c_5 = 218.357$, $c_6 = -198.887$, $c_7 = 51.1603$, $c_8 = 27.2838$, $c_9 = -1.58465$, and $c_{10} = -8.80071$.

APPENDIX D: SELECTION OF REFERENCE WAVE NUMBER k'_{ref}

Here, we describe why the reference wave number $k'_{\text{ref}} = 10$ was chosen in Fig. 4. As shown in Eq. (28), wave numbers satisfying $k' > k'_{\text{ref}}$ are used to estimate the degree of disagreement between two spectra. On the one hand, because the estimation is expected to be more accurate if we use as many wave numbers as possible, we want to use smaller k'_{ref} . On the other hand, when the wave numbers are too small, the scalar variance spectra are highly affected by the external source

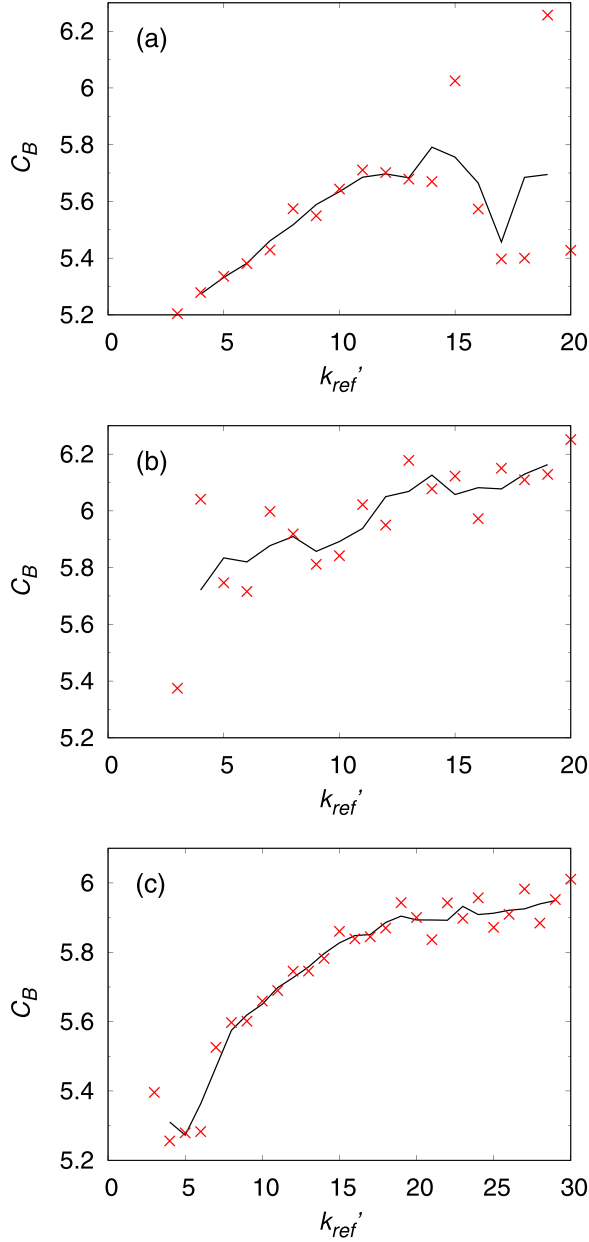


FIG. 18. Dependence of the estimation of C_B on choice of reference wave number k_{ref} (red crosses). The solid black curve indicates the moving average for three consecutive points. Panels (a), (b), and (c) are for Runs A, B, and C, respectively.

f_θ . Because such an effect is not assumed in the theory (10), including the external source effect degrades the estimation. Therefore, we want to use a greater k'_{ref} that is sufficiently far away from the forcing wave-number range ($1 \leq k' \leq 2$). Considering these two requirements, we changed k'_{ref} for Runs A–C and investigated its effect on C_B obtained from the fitting line in Fig. 5(a). The results are shown in Figs. 18(a), 18(b), and 18(c) for Runs A, B, and C, respectively. Although C_B fluctuates, it can be roughly said that it first increases with k'_{ref} for $k'_{\text{ref}} \geq 3$, then the rate of increase starts to slow

down around $10 < k'_{\text{ref}} < 15$, after which C_B fluctuates and increases slowly. From these results, we considered that the effect of the external source is sufficiently small for $k' > 10$, and therefore chose $k'_{\text{ref}} = 10$.

Note that, even if we use different k'_{ref} values (for example, $k'_{\text{ref}} = 11$), the conclusions from Fig. 5 do not change. Namely, the slope of the compensated spectrum α is proportional to D_K [$\alpha = (2C_B)D_K$], and C_B is consistent with the Batchelor constant directly estimated from the scalar variance spectrum in Fig. 6.

-
- [1] J. R. Taylor and R. Stocker, Trade-offs of chemotactic foraging in turbulent water, *Science* **338**, 675 (2012).
 - [2] R. Kubo, M. Toda, and N. Hashitsume, *Statistical Physics II Nonequilibrium Statistical Mechanics*, Series in Solid-State Sciences, Vol. 31 (Springer, Berlin, 1991).
 - [3] G. K. Batchelor, I. D. Howells, and A. A. Townsend, Small-scale variation of convected quantities like temperature in turbulent fluid Part 2. The case of large conductivity, *J. Fluid Mech.* **5**, 134 (1959).
 - [4] A. M. Obukhov, Structure of the temperature field in turbulent flows, *Isv. Akad. Nauk. SSSR, Ser. Geogr. Geophys.* **13**, 58 (1949).
 - [5] S. Corrsin, On the spectrum of isotropic temperature fluctuations in isotropic turbulence, *J. Appl. Phys.* **22**, 469 (1951).
 - [6] H. L. Grant, B. A. Hughes, W. M. Vogel, and A. Moilliet, The spectrum of temperature fluctuations in turbulent flow, *J. Fluid Mech.* **34**, 423 (1968).
 - [7] A. N. Oakey, Determination of the rate of dissipation of turbulent energy from simultaneous temperature and velocity shear microstructure measurements, *J. Phys. Oceanogr.* **12**, 256 (1982).
 - [8] K. Iwano, J. Hosoi, Y. Sakai, and Y. Ito, Power spectrum of high Schmidt number scalar in a turbulent jet at a moderate Reynolds number, *Exp. Fluids* **62**, 129 (2021).
 - [9] R. H. Kraichnan, Small-scale structure of a scalar field convected by turbulence, *Phys. Fluids* **11**, 945 (1968).
 - [10] R. H. Kraichnan, Convection of a passive scalar by a quasi-uniform random straining field, *J. Fluid Mech.* **64**, 737 (1974).
 - [11] Y. Kaneda, Inertial range structure of turbulent velocity and scalar fields in a Lagrangian renormalized approximation, *Phys. Fluids* **29**, 701 (1986).
 - [12] T. Gotoh, Passive scalar diffusion in two dimensional turbulence in the Lagrangian renormalized approximation, *J. Phys. Soc. Jpn.* **58**, 2365 (1989).
 - [13] P. K. Yeung, S. Xu, and K. R. Sreenivasan, Schmidt number effects on turbulent transport with uniform mean scalar gradient, *Phys. Fluids* **14**, 4178 (2002).
 - [14] D. Bogucki, J. A. Domaradzki, and P. K. Yeung, Direct numerical simulations of passive scalars with $Pr > 1$ advected by turbulent flow, *J. Fluid Mech.* **343**, 111 (1997).
 - [15] P. K. Yeung, S. Xu, D. A. Donzis, and K. R. Sreenivasan, Simulations of three-dimensional turbulent mixing for Schmidt numbers of the order 1000, *Flow, Turbul. Combust.* **72**, 333 (2004).
 - [16] T. Gotoh and P. K. Yeung, Passive scalar transport in turbulence, in *Ten Chapters in Turbulence*, edited by P. Davidson, Y. Kaneda, and K. R. Sreenivasan (Cambridge University Press, Cambridge, UK, 2011).
 - [17] K. P. Shete, D. J. Boucher, J. J. Riley, and S. M. de Bruyn Kops, Effect of viscous-convective subrange on passive scalar statistics at high Reynolds number, *Phys. Rev. Fluids* **7**, 024601 (2022).
 - [18] D. Buaria, M. P. Clay, K. R. Sreenivasan, and P. K. Yeung, Small-scale isotropy and ramp-cliff structures in scalar turbulence, *Phys. Rev. Lett.* **126**, 034504 (2021).
 - [19] D. Buaria, M. P. Clay, K. R. Sreenivasan, and P. K. Yeung, Turbulence is an ineffective mixer when Schmidt numbers are large, *Phys. Rev. Lett.* **126**, 074501 (2021).
 - [20] T. Gotoh, S. Hatanaka, and H. Miura, Spectral compact difference hybrid computation of passive scalar in isotropic turbulence, *J. Comput. Phys.* **231**, 7398 (2012).

- [21] T. Gotoh, T. Watanabe, and H. Miura, Spectrum of passive scalar at very high Schmidt number in turbulence, *Plasma Fusion Res.* **9**, 3401019 (2015).
- [22] M. P. Clay, D. Buaria, T. Gotoh, and P. K. Yeung, A dual communicator and dual grid-resolution algorithm for petascale simulations of turbulent mixing at high Schmidt number, *Comput. Phys. Commun.* **219**, 313 (2017).
- [23] M. P. Clay, D. Buaria, P. K. Yeung, and T. Gotoh, GPU acceleration of a petascale application for turbulent mixing at high Schmidt number using OpenMP 4.5, *Comput. Phys. Commun.* **228**, 100 (2018).
- [24] J.-B. Lagaert, G. Balarac, and G.-H. Cottet, Hybrid spectral-particle method for the turbulent transport of a passive scalar, *J. Comput. Phys.* **260**, 127 (2014).
- [25] P. Götzfried, M. S. Emran, E. Villiermaux, and J. Schumacher, Comparison of Lagrangian and Eulerian frames of passive scalar turbulent mixing, *Phys. Rev. Fluids* **4**, 044607 (2019).
- [26] T. Gotoh, I. Saito, and T. Watanabe, Spectra of supersaturation and liquid water content in cloud turbulence, *Phys. Rev. Fluids* **6**, 110512 (2021).
- [27] K. D. Squires and J. K. Eaton, Particle response and turbulence modification in isotropic turbulence, *Phys. Fluids* **2**, 1191 (1990).
- [28] M. Carbone, A. D. Bragg, and M. Iovieno, Multiscale fluid-particle thermal interaction in isotropic turbulence, *J. Fluid Mech.* **881**, 679 (2019).
- [29] I. Saito, T. Watanabe, and T. Gotoh, Modulation of fluid temperature fluctuations by particles in turbulence, *J. Fluid Mech.* **931**, A6 (2022).
- [30] K. Matsuda, R. Onishi, M. Hirahara, R. Kurose, K. Takahashi, and S. Komori, Influence of microscale turbulent droplet clustering on radar cloud observations, *J. Atmos. Sci.* **71**, 3569 (2014).
- [31] K. Matsuda, R. Onishi, and K. Takahashi, Influence of gravitational settling on turbulent droplet clustering and radar reflectivity factor, *Flow, Turbul. Combust.* **98**, 327 (2017).
- [32] K. Matsuda, K. Schneider, and K. Yoshimatsu, Scale-dependent statistics of inertial particle distribution in high Reynolds number turbulence, *Phys. Rev. Fluids* **6**, 064304 (2021).
- [33] T. Gotoh, T. Suehiro, and I. Saito, Continuous growth of cloud droplets in cumulus cloud, *New J. Phys.* **18**, 043042 (2016).
- [34] I. Saito and T. Gotoh, Turbulence and cloud droplets in cumulus clouds, *New J. Phys.* **20**, 023001 (2018).
- [35] T. Gotoh, D. Fukuyama, and T. Nakano, Velocity field statistics in homogeneous steady turbulence obtained using a high-resolution direct numerical simulation, *Phys. Fluids* **14**, 1065 (2002).
- [36] S. Sundaram and L. R. Collins, A numerical study of the modulation of isotropic turbulence by suspended particles, *J. Fluid Mech.* **379**, 105 (1999).
- [37] G. Jin, G.-W. He, and L.-P. Wang, Large-eddy simulation of turbulent collision of heavy particles in isotropic turbulence, *Phys. Fluids* **22**, 055106 (2010).
- [38] N. E.L. Haugen, A. Brandenburg, C. Sandin, and L. Mattsson, Spectral characterisation of inertial particle clustering in turbulence, *J. Fluid Mech.* **934**, A37 (2022).
- [39] D. A. Donzis, K. R. Sreenivasan, and P. K. Yeung, The Batchelor spectrum for mixing of passive scalars in isotropic turbulence, *Flow, Turbul. Combust.* **85**, 549 (2010).
- [40] Takeshi Watanabe and Toshiyuki Gotoh, Statistics of a passive scalar in homogeneous turbulence, *New J. Phys.* **6**, 40 (2004).
- [41] T. Gotoh and Y. Kaneda, Statistics of the inertial energy transfer range in d -dimensional turbulence ($2 \leq d \leq 3$) in a Lagrangian renormalized approximation, *Atmosphere* **14**, 1053 (2023).
- [42] A. Celani, A. Lanotte, A. Mazzino, and M. Vergassola, Fronts in passive scalar turbulence, *Phys. Fluids* **13**, 1768 (2001).
- [43] J. Bec, H. Homann, and G. Krstulovic, Clustering, fronts, and heat transfer in turbulent suspensions of heavy particles, *Phys. Rev. Lett.* **112**, 234503 (2014).
- [44] K. P. Iyer, J. Schumacher, K. R. Sreenivasan, and P. K. Yeung, Steep cliffs and saturated exponents in three-dimensional scalar turbulence, *Phys. Rev. Lett.* **121**, 264501 (2018).
- [45] S. Risius, H. Xu, F. D. Lorenzo, H. Xi, H. Siebert, R. A. Shaw, and E. Bodenschatz, Schneefernerhaus as a mountain research station for clouds and turbulence, *Atmos. Meas. Tech.* **8**, 3209 (2015).

- [46] H. Siebert, R. A. Shaw, J. Ditas, T. Schmeissner, S. P. Malinowski, E. Bodenschatz, and H. Xu, High-resolution measurement of cloud microphysics and turbulence at a mountaintop station, *Atmos. Meas. Tech.* **8**, 3219 (2015).
- [47] K. Karpinska, J. F. E. Bodenschatz, S. P. Malinowski, J. L. Nowak, S. Risius, T. Schmeissner, R. A. Shaw, H. Siebert, H. Xi, H. Xu, and E. Bodenschatz, Turbulence-induced cloud voids: Observation and interpretation, *Atmos. Chem. Phys.* **19**, 4991 (2019).
- [48] P. K. Yeung and S. B. Pope, An algorithm for tracking fluid particles in numerical simulations of homogeneous turbulence, *J. Comput. Phys.* **79**, 373 (1988).
- [49] P. K. Yeung, Lagrangian investigation of turbulence, *Annu. Rev. Fluid Mech.* **34**, 115 (2002).